AIAA SciTech Forum
8-12 January 2024, Orlando, FL
AIAA SCITECH 2024 Forum

10.2514/6.2024-0063

Improved Delayed Detached Eddy Simulation of Co-Flow Jet Flow Control in Extreme Adverse Pressure Gradients

B. McBreen,* Y.-C. Yang,† G.-C. Zha‡
Dept. of Mechanical and Aerospace Engineering
University of Miami, Coral Gables, Florida 33146
E-mail: gzha@miami.edu

Abstract

This paper conducts an Improved Delayed Detached Eddy Simulation (IDDES) as a high fidelity verification of flows with extreme adverse pressure gradients (EAPG), which are enabled by Co-Flow Jet (CFJ) active flow control (AFC). We define an EAPG to be an adverse pressure gradient that is at least ten times larger than the maximum adverse pressure gradient sustainable by the non-controlled flow of a baseline case at the same conditions. This paper simulates the flow around a CFJ6421-SST150-SUC247-INJ152 airfoil at an angle of attack (AoA) of 65° and a jet momentum coefficient (C_μ) of 2.5, which achieves a super-lift coefficient of $C_L = 9.58$. As a baseline for comparison, the NACA6421 airfoil is also simulated using IDDES at an AoA of 14°, at its $C_{L_{max}}$ condition just before stall. The simulation is conducted using FASIP, an in-house CFD program. The spatially filtered Navier-Stokes equations are solved using a fifth-order WENO reconstruction scheme for the inviscid fluxes and a fourth order central differencing scheme for the viscous fluxes. The CFJ airfoil demonstrates a remarkable ability to maintain attached flow at $\alpha = 65°$, generating an EAPG around the leading edge of the airfoil and immediately downstream of the injection slot. The CFJ airfoil achieves maximum streamwise and centrifugal pressure gradient coefficients 737 and 68 times higher than those of the baseline airfoil, respectively. This paper reinforces our understanding of the the CFJ's interaction with EAPGs, investigating the physical mechanisms underlying EAPG formation, and the CFJ's capacity to sustain attached flow within such conditions. Furthermore, it further validates the findings of our prior 2D URANS study, which first introduces the EAPG. Given its ability to maintain attached flow in the presence of an EAPG, the CFJ airfoil has the potential to be a promising and highly effective flow control device.

Nomenclature

AoA	Angle of Attack, α
AFC	Active Flow Control
APG	Adverse Pressure Gradient
CFJ	Co-Flow Jet
$CFWJ$	Co-Flow Wall Jet
$EAPG$	Extreme Adverse Pressure Gradient
$FASIP$	Flow-Acoustics-Structure Interaction Package
LE	Leading Edge
TE	Trailing Edge

* Ph.D. Candidate
† Ph.D.
‡ Professor, AIAA Associate Fellow

$ZNMF$	Zero-Net Mass Flux
PG_x	Normalized Streamwise Pressure Gradient, $\frac{C}{0.5\rho_\infty V_\infty^2}\frac{\partial p}{\partial x}$
PG_r	Normalized Radial Pressure Gradient, $\frac{C}{0.5\rho_\infty V_\infty^2}\frac{\partial p}{\partial r}$
PGR_x	Streamwise Pressure Gradient Ratio, $PG_x(CFJ)/PG_x(Baseline)$
PGR_r	Radial Pressure Gradient Ratio, $PG_r(CFJ)/PG_r(Baseline)$
P	CFJ pumping power consumption, $P = \frac{\dot{m}C_pT_{t2}}{\eta}(\Gamma^{\frac{\gamma-1}{\gamma}} - 1)$
η	CFJ pumping system efficiency
P_c	Power coefficient, $P_c = \frac{P}{\frac{1}{2}\rho_\infty V_\infty^3 S}$
PR	Total pressure ratio, Γ
C_L	Lift coefficient
C_D	Drag coefficient
C_μ	Jet momentum coefficient, $C_\mu = \frac{\dot{m}V_j}{\frac{1}{2}\rho_\infty {V_\infty}^2 S}$
$C_{L_{max}}$	Maximum lift coefficient
$(C_L/C_D)_c$	Aerodynamic efficiency corrected for CFJ airfoil, $\frac{L}{D+P/V_\infty}$
Re	Reynolds number
Ma	Mach number
C_p	Pressure coefficient
γ	Air specific heat ratio
ρ_∞	Freestream density
V_∞	Freestream velocity
T_t	Total temperature
P_t	Total pressure
H_t	Total specific enthalpy
$\dot{m}$	Mass flow rate through the pump
ω_z	Spanwise Vorticity
C, c	Chord length
r_c	Radius of Curvature
κ	Curvature, $1/r_c$
$\bar{f}$	Reduced Frequency, fL/U

1 Introduction

Active Flow Control (AFC) may substantially extend the operating limits of a flow system by sustaining a higher maximum adverse pressure gradient (APG) within the flow. When the maximum adverse pressure gradient exceeds ten times the maximum APG that its non-controlled counterpart flow can sustain, we refer to it as an Extreme Adverse Pressure Gradient (EAPG). Two-dimensional simulation of Co-Flow Jet (CFJ) active flow control using Unsteady Reynolds Averaged Navier-Stokes (URANS) equations has indicated that a CFJ airfoil is able to achieve and sustain an EAPG [1, 2], reaching extraordinary adverse pressure gradient magnitudes. The maximum lift coefficient of an airfoil is governed by the maximum adverse pressure gradient that airfoil can sustain before stalling. That being so, using AFC to increase an airfoil's APG limit will expand the operating range of those fluid systems. Many fluid systems rely on airfoils such as aircraft, wind turbines, turbomachinery, etc. Studying EAPGs' potential to enhance the capability of airfoils or other similar flow control devices therefore has broad practical significance. On the theoretical side, this exploration into extreme adverse pressure gradients lays the groundwork for a research of a flow domain not well documented in fluid dynamics literature.

1.1 CoFlow Jet and EAPG Flow

The Co-Flow Jet is a zero-net-mass-flux active flow control method that uses fluidic actuators developed by Zha and his team [3, 4, 5, 6, 7, 8, 9, 10, 11, 12, 10, 2, 13, 14, 15, 16]. The CFJ airfoil has a tangential injection slot near the leading edge of the airfoil's suction surface and a streamwise suction slot near the trailing edge, shown in Fig. 1. A small amount of flow is ingested into the airfoil through the suction slot, pressurized and energized by a micro-compressor inside the airfoil, then injected near the leading edge through the injection slot. The Co-Flow Jet injection is a wall jet because of its tangential injection vector. Since CFJ jet injection usually destabilizes the flow, Co-Flow Jet wall jets are categorized as turbulent wall jets [17].

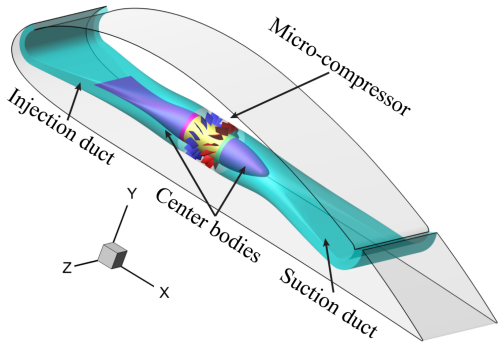

Figure 1: Schematic of components making up CFJ airfoil.

Yang and Zha [2] first observed in their 2D RANS simulation study that a CFJ-NACA6421 airfoil can sustain lifting flow at AoA up to 70° without stall, generating lift coefficients far exceeding the maximum lift coefficient limit derived by Smith [18]. Smith postulated that an airfoil's maximum theoretical lift would occur at an AoA of 90°, with magnitude $C_{L_{max}} = 2\pi(1 + t/c)$. This premise is based on potential flow theory. Yang and Zha further observed that the high circulation generated by the CFJ causes the rear stagnation point to detach from the airfoil's solid body. The CFJ airfoil Yang and Zha studied employs a very thin injection slot, which effectively generates a very high lift coefficient, but also requires very high power to actuate the CFJ. Wang and Zha [19, 20] modified the CFJ airfoil by enlarging the injection and suction slot sizes. Their airfoil design maintains the capability of achieving very high lift coefficients but substantially reduces the CFJ required power. According to their simulation, Wang and Zha's airfoil is able to attach flow up to AoA 80° [19]. According to Smith's maximum lift theory, the 21% thickness CFJ-NACA6421 airfoil should have a $C_{L_{max}}$ of 7.6, but Wang and Zha's 2D RANS study showed lift coefficients as high as 16.5, more than doubling the $C_{L_{max}}$ limit. A lift coefficient exceeding Smith's $C_{L_{max}}$ is termed a "Super-Lift Coefficient" (SLC) [2]. The CFJ6421 airfoil has been shown to generate a SLC by wind tunnel testing, with a lift coefficient of 8.6 [13]. For the present study, the injection slot is 30% larger than Wang and Zha's design [19, 20] and the injection duct curvature is reduced to accommodate subsonic injection flow at high C_μ and very high angles of attack [1].

The pressure gradient coefficient in the streamwise and centrifugal directions are defined in [1] as:

$$PG_x = \frac{C}{0.5\rho_\infty V_\infty^2}\frac{\partial p}{\partial x}, \quad PG_r = \frac{C}{0.5\rho_\infty V_\infty^2}\frac{\partial p}{\partial r} \approx \frac{C}{0.5\rho_\infty V_\infty^2}\frac{\rho V_t^2}{R} \tag{1}$$

where the subscript x denotes the streamwise direction, r denotes the direction normal to the wall and transverse to the flow, C is the airfoil chord, V_t is the tangential velocity, and R is the local radius of curvature.

McBreen et al. [1] examined the maximum streamwise adverse pressure gradient and centrifugal pressure gradient coefficients of the 2D CFJ-NACA6421 airfoil at super-lift conditions using URANS. They found that the CFJ augments the adverse and centrifugal pressure gradients by 3 and 2 orders of magnitude respectively compared to the non-controlled baseline NACA6421 airfoil. Thus the 2D URANS results achieve EAPG [1]. Xu et al. [17] simulated the widely studied NASA hump using 2D URANS, implementing a "Co-Flow Wall Jet" (CFWJ) to attach the flow in the hump's adverse pressure gradient. Xu et al. dissected the physical mechanisms responsible for offsetting the APG to maintain flow attachment, concluding that the injection jet mass flux, streamwise vorticity, and turbulent diffusion are the three factors responsible for offsetting the APG. In particular, turbulent diffusion plays a dominant role among the three factors. However, the NASA hump does not generate an EAPG when the flow is attached by the CFWJ. It is not certain if the mechanism observed in the 2D RANS simulation with mild APG can be fully applied to flows with an EAPG.

Study of the EAGP phenomenon so far has led to many questions. Is the EAPG an artifact of the Spalart-Allmaras (SA) one-equation turbulence model [21] in a 2D URANS simulation? The SA-RANS turbulence model is known to have limited accuracy because of its treatment of eddies as isotropic structures with universal scale filtering. The questions to be asked are as follows: 1) Is the EAPG obtained by 2D URANS qualitatively correct? 2) Since the RANS model is not designed to sustain EAPG [21], is the turbulent diffusion and transport predicted by RANS simulations reasonable? 3) Is the EAPG only a 2D phenomenon or is it also observed with 3D flow structures? 4) What is the physical mechanism enabling CFJ flow to sustain extreme adverse pressure gradients? 5) Does the trailing edge detached stagnation point exist in the 3D viscous flow field? Thoroughly answering these questions requires considerable effort, including more sophisticated Large Eddy Simulation (LES), Direct Numerical Simulation (DNS), and experimental studies.

The purpose of this paper is to take one step beyond the 2D URANS study by using 3D Improved Delayed Detached Eddy Simulation (IDDES) to further verify the CFJ's EAPG phenomenon. IDDES is a hybrid RANS/LES model evolved from the Detached Eddy Simulation (DES) model under a series of developments by Spalart et al. [22, 23, 24]. IDDES resolves the non-isotropic large eddies outside of boundary layer by using LES, but adopts the RANS model within the wall boundary layer. It is thus still limited to the Boussinesq eddy viscosity assumption within the boundary layer. The turbulence behavior very near the wall may not be adequately resolved. However, 3D IDDES provides considerably more insight into the flow physics of CFJ EAPG flows than 2D UARNS. Previous studies indicate that the IDDES and DES predicts the massive separated flow with significantly improved accuracy over URANS quantitatively and qualitatively [25, 26, 27, 28, 29, 11]. Numerical results for the CFJ airfoil with EAPG at AoA of 65° are compared to the 3D baseline NACA6421 airfoil at 14° AoA, its $C_{L_{max}}$ condition.

2 Numerical Algorithms

The IDDES solver implemented and validated by Yang and Zha [25, 30] is adopted in this study.

2.1 Governing Equations

The spatially filtered Navier-Stokes governing equations in generalized coordinates are expressed as:

$$\frac{\partial \mathbf{Q}}{\partial t}+\frac{\partial \mathbf{E}}{\partial \xi}+\frac{\partial \mathbf{F}}{\partial \eta}+\frac{\partial \mathbf{G}}{\partial \zeta}=\frac{1}{Re}\left(\frac{\partial \mathbf{E}_v}{\partial \xi}+\frac{\partial \mathbf{F}_v}{\partial \eta}+\frac{\partial \mathbf{G}_v}{\partial \zeta}+\mathbf{S}\right) \tag{2}$$

where Re is the Reynolds number. The equations are normalized based on airfoil chord L_∞, freestream density ρ_∞ and velocity U_∞.

The conservative variable vector $\mathbf{Q}$, the inviscid flux vectors $\mathbf{E}$, $\mathbf{F}$, $\mathbf{G}$, the viscous flux $\mathbf{E_v}$, $\mathbf{F_v}$, $\mathbf{G_v}$ and the source term vector $\mathbf{S}$ are expressed as

$$\mathbf{Q}=\frac{1}{J}\begin{pmatrix}\bar{\rho}\\ \bar{\rho}\tilde{u}\\ \bar{\rho}\tilde{v}\\ \bar{\rho}\tilde{w}\\ \bar{\rho}\tilde{e}\\ \bar{\rho}\tilde{\nu}_t\end{pmatrix},\mathbf{E}=\begin{pmatrix}\bar{\rho}U\\ \bar{\rho}\tilde{u}U+l_x\bar{p}\\ \bar{\rho}\tilde{v}U+l_y\bar{p}\\ \bar{\rho}\tilde{w}U+l_z\bar{p}\\ \left(\bar{\rho}\tilde{e}+\bar{p}\right)U-l_t\bar{p}\\ \bar{\rho}\tilde{\nu}U\end{pmatrix},\mathbf{F}=\begin{pmatrix}\bar{\rho}V\\ \bar{\rho}\tilde{u}V+m_x\bar{p}\\ \bar{\rho}\tilde{v}V+m_y\bar{p}\\ \bar{\rho}\tilde{w}V+m_z\bar{p}\\ \left(\bar{\rho}\tilde{e}+\bar{p}\right)V-m_t\bar{p}\\ \bar{\rho}\tilde{\nu}V\end{pmatrix},\mathbf{G}=\begin{pmatrix}\bar{\rho}W\\ \bar{\rho}\tilde{u}W+n_x\bar{p}\\ \bar{\rho}\tilde{v}W+n_y\bar{p}\\ \bar{\rho}\tilde{w}W+n_z\bar{p}\\ \left(\bar{\rho}\tilde{e}+\bar{p}\right)W-n_t\bar{p}\\ \bar{\rho}\tilde{\nu}W\end{pmatrix} \tag{3}$$

$$\mathbf{E_v}=\begin{pmatrix}0\\ l_k\bar{\tau}_{xk}\\ l_k\bar{\tau}_{yk}\\ l_k\bar{\tau}_{zk}\\ l_k\left(\tilde{u}_i\bar{\tau}_{ki}-\bar{q}_k\right)\\ \frac{\bar{\rho}}{\sigma}\left(\nu+\tilde{\nu}\right)\left(\mathbf{l}\bullet\nabla\tilde{\nu}\right)\end{pmatrix},\mathbf{F_v}=\begin{pmatrix}0\\ m_k\bar{\tau}u_{xk}\\ m_k\bar{\tau}_{yk}\\ m_k\bar{\tau}u_{zk}\\ m_k\left(\tilde{u}_i\bar{\tau}_{ki}-\bar{q}_k\right)\\ \frac{\bar{\rho}}{\sigma}\left(\nu+\tilde{\nu}\right)\left(\mathbf{m}\bullet\nabla\tilde{\nu}\right)\end{pmatrix},\mathbf{G_v}=\begin{pmatrix}0\\ n_k\bar{\tau}_{xk}\\ n_k\bar{\tau}_{yk}\\ n_k\bar{\tau}_{zk}\\ n_k\left(\tilde{u}_i\bar{\tau}_{ki}-\bar{q}_k\right)\\ \frac{\bar{\rho}}{\sigma}\left(\nu+\tilde{\nu}\right)\left(\mathbf{n}\bullet\nabla\tilde{\nu}\right)\end{pmatrix} \tag{4}$$

$$\mathbf{S}=\frac{1}{J}\begin{pmatrix}0\\ 0\\ 0\\ 0\\ 0\\ S_\nu\end{pmatrix} \tag{5}$$

where ρ is the density, p is the static pressure, and e is the total energy per unit mass. The overbar denotes a regular filtered variable in the LES region, or a Reynolds-averaged value in the RANS region. The tilde symbol is used to denote Favre filtered variables. ν is kinematic viscosity and $\tilde{\nu}$ is the working variable related to eddy viscosity in the S-A and IDDES turbulence one equation model [21]. U, V and W are the contravariant velocities in ξ, η, ζ directions, and defined as

$$\begin{aligned}U&=l_t+\mathbf{l}\bullet\mathbf{V}=l_t+l_x\tilde{u}+l_y\tilde{v}+l_z\tilde{w}\\ V&=m_t+\mathbf{m}\bullet\mathbf{V}=m_t+m_x\tilde{u}+m_y\tilde{v}+m_z\tilde{w}\\ W&=n_t+\mathbf{n}\bullet\mathbf{V}=n_t+n_x\tilde{u}+n_y\tilde{v}+n_z\tilde{w}\end{aligned} \tag{6}$$

where J is the Jacobian of the coordinate transformation. l_t, m_t and n_t are the components of the interface contravariant velocity of the grid in ξ, η and ζ directions respectively. $\mathbf{l}$, $\mathbf{m}$ and $\mathbf{n}$ denote the normal vectors located at the centers of ξ, η and ζ interfaces of the control volume with their magnitudes equal to the surface areas and pointing to the directions of increasing ξ, η and ζ.

$$\mathbf{l} = \frac{\nabla\xi}{J},\ \mathbf{m} = \frac{\nabla\eta}{J},\ \mathbf{n} = \frac{\nabla\zeta}{J} \tag{7}$$

$$l_t = \frac{\xi_t}{J},\ m_t = \frac{\eta_t}{J},\ n_t = \frac{\zeta_t}{J} \tag{8}$$

In the generalized coordinates, $\Delta\xi = \Delta\eta = \Delta\zeta = 1$. Since the DES-family approach is based on S-A model, the formulations of the original S-A model are give below. The source term S_ν from the S-A model in Eq. 5, is given by

$$\begin{aligned} S_\nu = \bar{\rho}C_{b1}\left(1-f_{t2}\right)\tilde{S}\tilde{\nu} + \tfrac{1}{Re}\left[-\bar{\rho}\left(C_{w1}f_w - \tfrac{C_{b1}}{\kappa^2}f_{t2}\right)\left(\tfrac{\tilde{\nu}}{d}\right)^2\right. \\ \left. +\tfrac{\bar{\rho}}{\sigma}C_{b2}\left(\nabla\tilde{\nu}\right)^2 - \tfrac{1}{\sigma}\left(\nu+\tilde{\nu}\right)\nabla\tilde{\nu}\bullet\nabla\bar{\rho}\right] + Re\left[\bar{\rho}f_{t1}\left(\Delta q\right)^2\right] \end{aligned} \tag{9}$$

where

$$\chi = \frac{\tilde{\nu}}{\nu}, \quad f_{v1} = \frac{\chi^3}{\chi^3 + c_{v1}^3}, \quad f_{v2} = 1 - \frac{\chi}{1+\chi f_{v1}}, \quad f_{t1} = C_{t1}g_t exp\left[-C_{t2}\frac{\omega_t^2}{\Delta U^2}\left(d^2 + g_t^2 d_t^2\right)\right] \tag{10}$$

$$f_{t2} = C_{t3}exp\left(-C_{t4}\chi^2\right), \quad f_w = g(\frac{1+c_{w3}^6}{g^6+c_{w3}^6})^{1/6}, \quad g = r + c_{w2}(r^6 - r) \tag{11}$$

$$g_t = min\left(0.1, \frac{\Delta q}{\omega_t \Delta x_t}\right), \quad \tilde{S} = S + \frac{\tilde{\nu}}{k^2 d^2 R_e}f_{v2}, \quad r = \frac{\tilde{\nu}}{\tilde{S}k^2 d^2 R_e} \tag{12}$$

where, ω_t is the wall vorticity at the wall boundary layer trip location, d is the distance to the closest wall, d_t is the distance of the field point to the trip location, Δq is the difference of the velocities between the field point and the trip location, Δx_t is the grid spacing along the wall at the trip location. The values of the coefficients are: $c_{b1} = 0.1355, c_{b2} = 0.622, \sigma = \frac{2}{3}, c_{w1} = \frac{c_{b1}}{k^2} + (1+c_{b2})/\sigma, c_{w2} = 0.3, c_{w3} = 2, k = 0.41, c_{v1} = 7.1, c_{t1} = 1.0, c_{t2} = 2.0, c_{t3} = 1.1, c_{t4} = 2.0$.

The shear stress $\bar{\tau}_{ik}$ and total heat flux $\bar{q}_k$ in Cartesian coordinates is given by

$$\bar{\tau}_{ik} = \left(\mu + \mu_{IDDES}\right)\left[\left(\frac{\partial\tilde{u}_i}{\partial x_k} + \frac{\partial\tilde{u}_k}{\partial x_i}\right) - \frac{2}{3}\delta_{ik}\frac{\partial\tilde{u}_j}{\partial x_j}\right] \tag{13}$$

$$\bar{q}_k = -\left(\frac{\mu}{Pr} + \frac{\mu_{IDDES}}{Pr_t}\right)\frac{\partial\tilde{T}}{\partial x_k} \tag{14}$$

where μ is from Sutherland's law. For IDDES approach in general, the eddy viscosity is represented by $\mu_{IDDES}(= \bar{\rho}\tilde{\nu}f_{v1})$.

2.2 Improved Delayed Detached Eddy Simulation (IDDES)

The Improved DDES (IDDES) is introduced by extending the DDES with the WMLES capacity. The IDDES has two branches, DDES and WMLES, including a set of empirical functions of subgrid length-scales designed to achieve good performance from these branches themselves and their coupling. By switching the activation of RANS and LES in different flow regions, IDDES significantly expands the scope of application of DDES with well-balanced and powerful numerical approach to complex turbulent flows at high Reynolds numbers.

2.2.1 DDES branch of IDDES

The DDES branch is responsible for the DDES-like functionality of IDDES and should become active only when the inflow conditions do not have any turbulent content (if a simulation has spatial periodicity, the initial conditions rather than the inflow conditions set the characteristics of the simulation), in particular when a grid of "boundary-layer type" precludes the resolution of the dominant eddies. The DDES formulation can be reformulated as

$$l_{DDES} = l_{RANS} - f_d max\{0, l_{RANS} - l_{LES}) \tag{15}$$

where the delaying function, f_d, is defined the same as

$$f_d = 1 - tanh[(8r_d)^3] \tag{16}$$

and the quantity r_d borrowed from the S-A RANS turbulence model:

$$r_d = \frac{\nu_t + \nu}{k^2 d_w^2 max[(U_{i,j}U_{i,j})^{0.5}, 10^{-10}]} \tag{17}$$

is a marker of the wall region, which is equal to 1 in a log layer and 0 in a free shear flow.

In Eq. 17, $U_{i,j}$ represents the velocity gradient, and k denotes the Karmann constant. Based on the general DES concept, in order to create a seamless hybrid model, the length-scale IDDES defined by Eq.15 is substituted into the background RANS model to replace the RANS length-scale, l_{RANS}, which is explicitly or implicitly involved in any such model. For instance, for the S-A model the length-scale is equal to the distance to the wall $l_{RANS} = d_w$. In the original DES97, the length-scale depends only on the local grid. In DDES and IDDES, it also depends on the solution of Eq. 15 and 17.

The LES length-scale, l_{LES}, is defined via the subgrid length-scale for Eq. 15 as

$$l_{LES} = C_{DES}\Phi\Delta \tag{18}$$

where C_{DES} is the fundamental empirical constant of DES, 0.65. Φ is a low-Reynolds number correction introduced in order to compensate the activation of the low-Reynolds number terms of some background RANS model in LES mode. Both C_{DES} and Φ depend on the background RANS model, and Ψ is equal to 1 if the RANS model does not include any low-Reynolds number terms.

2.2.2 WMLES branch of IDDES

The WMLES branch is intended to be active only when the inflow conditions used in the simulation are unsteady and impose some turbulent content with the grid fine enough to resolve boundary-layer dominant eddies. It presents a new seamless hybrid RANS-LES model, which couples RANS and LES approaches via the introduction of the following blended RANS-LES length-scale:

$$l_{WMLES} = f_B(1 + f_e)l_{RANS} + (1 - f_B)l_{LES} \tag{19}$$

The empirical blending-function f_B depends upon d_w/h_{max} and is defined as

$$f_B = min\{2exp(-9\alpha^2), 1.0\}, \alpha = 0.25 - d_w/h_{max} \tag{20}$$

It varies from 0 to 1 and provides rapid switching of the model from RANS mode ($f_B = 1.0$) to LES mode ($f_B = 0$) within the range of wall distance $0.5h_{max} < d_w < h_{max}$

The second empirical function involved in Eq. 19, elevating-function, f_e, is aimed at preventing the excessive reduction of the RANS Reynolds stresses observed in the interaction of the RANS and LES regions in the vicinity of their interface. It is intended to eliminating the log-layer mismatch (LLM) problem.

$$f_e = max\{(f_{e1} - 1), 0\}\Phi f_{e2} \tag{21}$$

where the function f_{e1} is defined as

$$f_{e1}(d_w/h_{max}) = \begin{cases} 2exp(-11.09\alpha^2) & \text{if } \alpha \geq 0 \\ 2exp(-9.0\alpha^2) & \text{if } \alpha < 0 \end{cases} \tag{22}$$

It provides a grid-dependent "elevating" device for the RANS component of the WMLES length-scale.

The function f_{e2} is: $$f_{e2} = 1.0 - max\{f_t, f_l\} \tag{23}$$

2.2.3 Blending DDES and WMLES branches

The DDES length-scale defined by Eq. 15 and that of the WMLES-branch defined by Eq. 19 do not blend directly in a way to ensure an automatic choice of the WMLES or DDES mode by the combined model, depending on the type of the simulation (with or without turbulent content) and the grid used.

However a modified version of equivalent length scale combination, namely,

$$\tilde{l}_{DDES} = \tilde{f}_d l_{RANS} + (1 - \tilde{f}_d)l_{LES} \tag{24}$$

where the blending function $\tilde{f}_d$ is defined by

$$\tilde{f}_d = max\{(1 - f_{dt}), f_B\} \tag{25}$$

with $f_{dt} = 1 - tanh[(8r_{dt})^3]$

With the use of Eq. 24, the required IDDES length-scale combining the DDES and WMLES length scales defined by Eqns. 24 and 19 is straightforward and can be implemented as

$$l_{hyb} = \tilde{f}_d(1 + f_e)l_{RANS} + (1 - \tilde{f}_d)l_{LES} \tag{26}$$

With inflow turbulent content, f_{dt} is close to 1.0, $\tilde{f}_d$ is equal to f_B, so Eq. 26 is reduced to $l_{hyb} = l_{WMLES}$ in Eq. 19. Otherwise, f_e is zero, Eq. 26 is interpreted as $l_{hyb} = l_{DDES}$ in Eq. 24.

2.3 Time Marching Scheme

Following the dual time stepping method suggested by Jameson [31], an implicit pseudo time marching scheme using line Gauss-Seidel line relaxation is employed to solve the governing equations, as the following:

$$\frac{\partial \mathbf{Q}}{\partial t} = \frac{3\mathbf{Q^{n+1}} - 4\mathbf{Q^n} + \mathbf{Q^{n-1}}}{2\Delta t} \tag{27}$$

where $n-1$, n and $n+1$ are three sequential time levels, which have a time interval of Δt. The first-order Euler scheme is used to discretize the pseudo temporal term. The semi-discretized equations of the governing equations are given as the following:

$$\begin{aligned} &\left[\left(\tfrac{1}{\Delta\widehat{\tau}} + \tfrac{1.5}{\Delta t}\right) I - \left(\tfrac{\partial R}{\partial \mathbf{Q}}\right)^{n+1,m}\right] \delta\mathbf{Q^{n+1,m+1}} \\ &\quad = R^{n+1,m} - \tfrac{3\mathbf{Q^{n+1,m}} - 4\mathbf{Q^n} + \mathbf{Q^{n-1}}}{2\Delta t} \end{aligned} \tag{28}$$

where the $\Delta\widehat{\tau}$ is the pseudo time step, and R stands for the net flux determined by the spatial high order numerical scheme, m is the iteration index for the pseudo time.

2.4 Navier-Stokes Solver

The in-house high order accuracy CFD code Flow-Acoustics-Structure Interaction Package (FASIP) is used to conduct the numerical simulation. The 3D Navier-Stokes equations given Section 2.1 are solved by a 5th order WENO scheme for the inviscid flux [32, 33, 34] and a 4th order central differencing for the viscous terms [33]. The low diffusion E-CUSP scheme used as the approximate Riemann solver suggested by Zha et al [35] based on the Zha-Bilgen flux-vector-splitting scheme [36] is utilized with the WENO scheme to evaluate the inviscid fluxes. Implicit time marching method using Gauss-Seidel line relaxation is used to achieve a fast convergence rate [37]. Parallel computing is implemented to save simulation time [38]. The FASIP code is intensively validated for CFJ flow control simulations [15, 10, 11, 12, 14, 7, 3, 16, 39].

2.5 CoFlow Jet Parameters

2.5.1 Jet Momentum Coefficient

The jet momentum coefficient C_μ is a parameter used to quantify the injection intensity. It is defined as :

$$C_\mu = \frac{\dot{m} V_j}{\frac{1}{2}\rho_\infty {V_\infty}^2 S} \tag{29}$$

where $\dot{m}$ is the injection mass flow, V_j the injection velocity, ρ_∞ and V_∞ denote the free stream density and velocity, and S is the planform area.

2.5.2 Pumping Power

The CFJ is implemented via a pumping system inside the wing that draws air from the suction slot and blows it out of the injection slot. As a Zero-Net-Mass-Flux (ZNMF) flow control mechanism with a closed flow path, the CFJ power required can be defined by the thermodynamic relationship based on the mass flow rate and total enthalpy variation as the following:

$$P = \dot{m}(H_{t1} - H_{t2}) \tag{30}$$

where H_{t1} and H_{t2} are the total enthalpy in the injection cavity and suction cavity respectively, P is the Power required by the pump and $\dot{m}$ the jet mass flow rate. Introducing the pumping efficiency η and total pressure ratio of the pump $\Gamma = \frac{P_{t1}}{P_{t2}}$, the power consumption can be expressed as :

$$P = \frac{\dot{m} C_p T_{t2}}{\eta}(\Gamma^{\frac{\gamma-1}{\gamma}} - 1) \tag{31}$$

The power consumption can be expressed as a power coefficient below:

$$P_c = \frac{P}{\frac{1}{2}\rho_\infty V_\infty^3 S} \tag{32}$$

In this research, the CFJ pumping efficiency is set to 100% to calculate the power required. This choice is discussed further in Section 4. Eq. 31 indicates that the power required by the CFJ is determined linearly by the mass flow rate and exponentially by the total pressure ratio. Large injection slots reduce the power required because the total pressure loss in the injection duct is substantially reduced. It follows that the most efficient way to implement the CFJ is to employ a large mass flow rate and low total pressure ratio.

2.5.3 Corrected Aerodynamic Efficiency

The conventional airfoil aerodynamic efficiency is defined as C_L/C_D. However since CFJ active flow control consumes energy, the CFJ corrected aerodynamic efficiency is modified to take into account the energy consumption of the pump. The formulation of the corrected aerodynamic efficiency for CFJ airfoils is :

$$\left(\frac{C_L}{C_D}\right)_c = \frac{L}{D + \frac{P}{V_\infty}} = \frac{C_L}{C_D + P_C} \tag{33}$$

where V_∞ is the free stream velocity, P is the CFJ pumping power, and L and D are the lift and drag generated by the CFJ airfoil. This formulation effectively converts the power consumed by the CFJ into drag for the airfoil.

2.5.4 Lift and Drag Calculation

The momentum and pressure at the injection and suction slots produce a reactionary force not included in the surface integral used to calculate lift and drag on the airfoil surface. Using control volume analysis (Fig. 2), the reactionary force can be calculated using the flow parameters at the injection and suction slot opening surfaces. Zha et al. [3] give the following formulations to calculate the lift and drag due to the jet reactionary force for a CFD simulation. By considering the effects of injection and suction jets on the CFJ airfoil, the expressions for these reactionary forces are given as:

$$F_{x_{cfj}} = (\dot{m}_j V_{j1} + p_{j1} A_{j1}) * \cos(\theta_1 - \alpha) - (\dot{m}_j V_{j2} + p_{j2} A_{j2}) * \cos(\theta_2 + \alpha) \tag{34}$$

$$F_{y_{cfj}} = (\dot{m}_{j1} V_{j1} + p_{j1} A_{j1}) * \sin(\theta_1 - \alpha) + (\dot{m}_{j2} V_{j2} + p_{j2} A_{j2}) * \sin(\theta_2 + \alpha) \tag{35}$$

where the subscripts 1 and 2 stand for the injection and suction respectively, and θ_1 and θ_2 are the angles between the injection and suction slot surfaces and a line normal to the airfoil chord. α is the angle of attack.

The total lift and drag on the airfoil can then be expressed as:

$$D = R'_x - F_{x_{cfj}} \tag{36}$$

$$L = R'_y - F_{y_{cfj}} \tag{37}$$

where R'_x and R'_y are the surface integral of pressure and shear stress in x (drag) and y (lift) direction excluding the internal ducts of injection and suction. For the CFD simulation, the total lift and drag are calculated using Eqns. 36 and 37. The above terms are sketched in Figure 2.

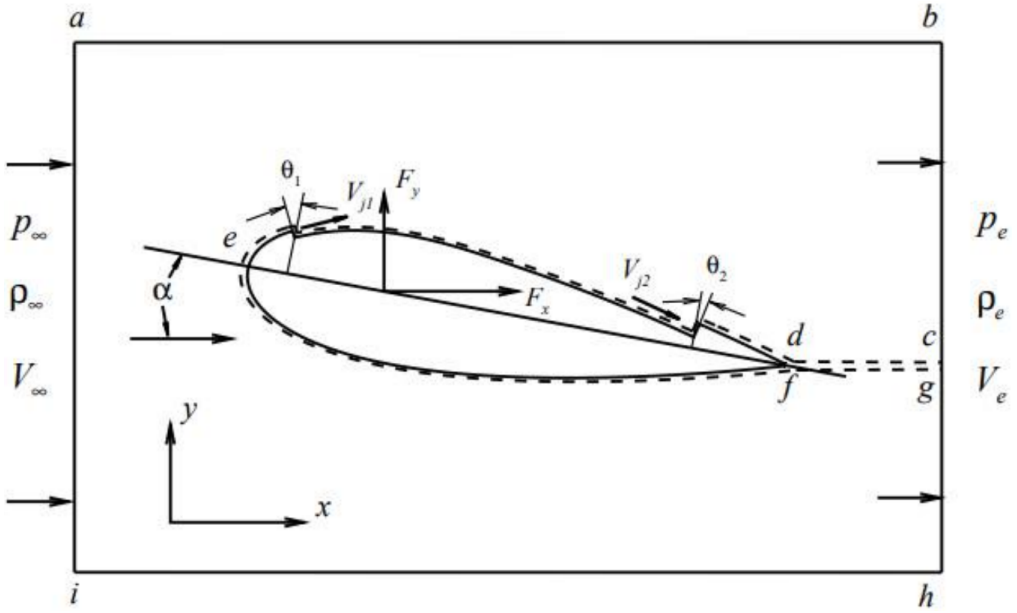

Figure 2: Control-volume diagram of CFJ airfoil.

2.6 Computational Mesh and Flow Conditions

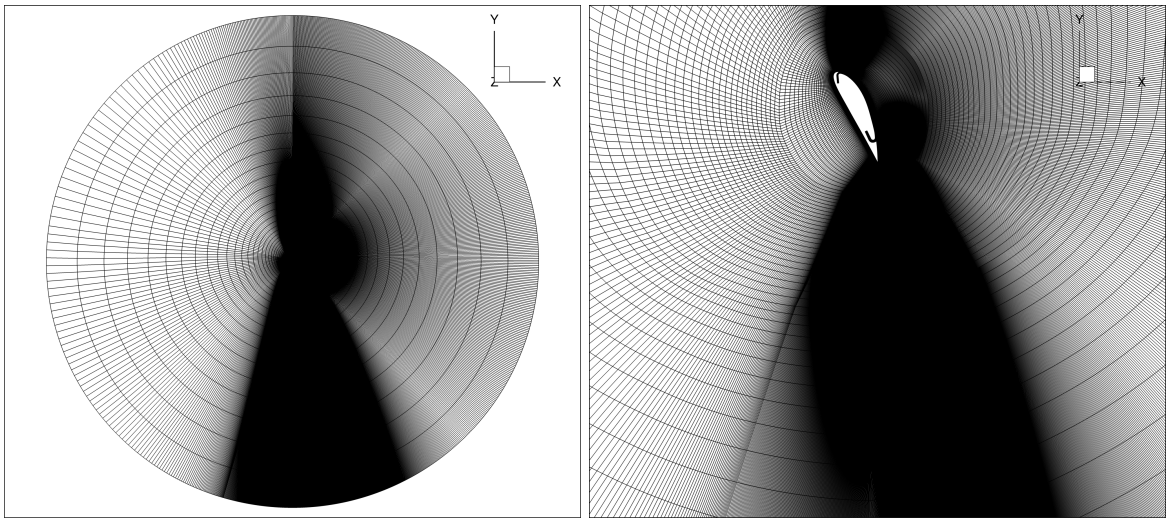

Figure 3: Computational mesh for CFJ airfoil far field with additional cells to resolve the wake.

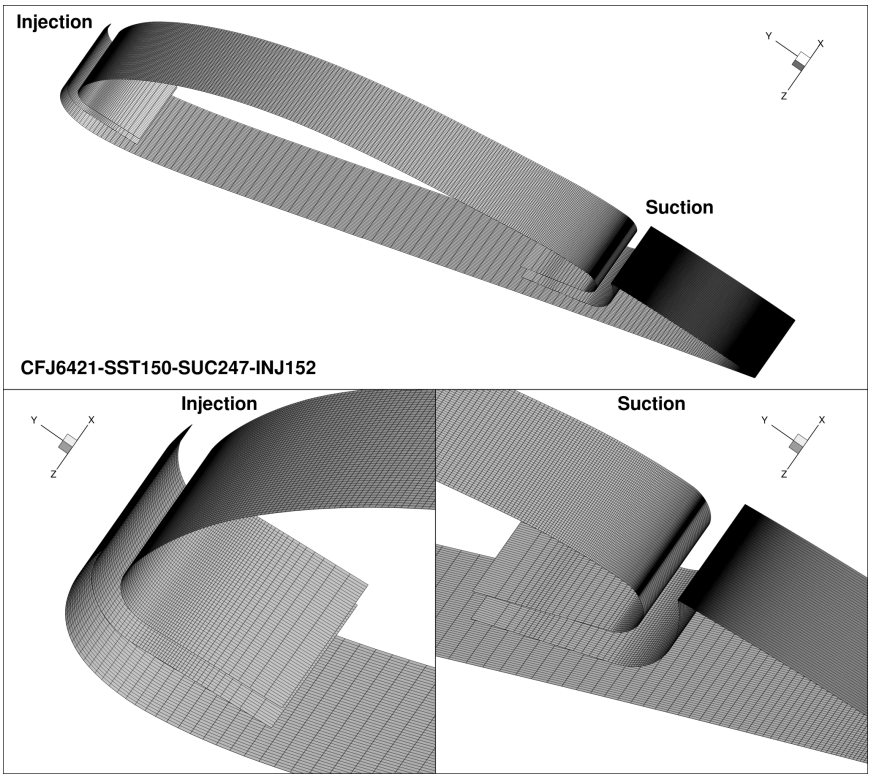

Figure 4: CFJ airfoil surface mesh.

The 3D multiblock structured meshes for the baseline and CFJ airfoils are constructed using an O-mesh topology in order to achieve high mesh quality near airfoil wall surfaces. The simulated CFJ wing span is 10% the chord length, with periodic boundary conditions applied on the spanwise domain faces. For the CFJ airfoil mesh, 2001 grid points are distributed circumferentially around the airfoil, with 601 points on the lower surface and 1401 points on the upper surface, 301 points distributed radially from the airfoil, and 51 points in the spanwise direction. For

the CFJ slots and suction surface translation region, there are 61 points distributed across the jet. The total mesh size is 14,600,000 cells and is partitioned into 308 blocks for parallel computation. The far-field boundary is 200 chords away from the airfoil radially. To resolve the turbulent boundary layer, the first grid point is placed at or below $y^+ \approx 1$. The flow parameters and mesh dimensions are given in the table below. The cross section mesh showing the far field and local region around the airfoil is shown in Fig. 3. The mesh is refined in the wake region to better resolve the turbulent wake flow. The surface mesh for the CFJ airfoil is shown in Fig. 4. Table 1 lists the mesh size and the freestream conditions.

Table 1: Mesh and freestream flow parameters

Case	Mach	Reynolds	Mesh $N_\xi \times N_\eta \times N_\zeta$
Baseline	0.063	5.62×10^5	$1600 \times 175 \times 50$
CFJ	0.063	5.62×10^5	$2000 \times 300 \times 50^*$

* The grid points around the airfoil exclude the CFJ injection and suction blocks.

For the IDDES simulation, a normalized physical time step of 3.0×10^{-4} is used, and a CFL number of 10 is applied for the pseudo time iteration. The freestream Mach number is 0.063 and freestream Reynolds number is 5.62×10^5. The jet momentum coefficient C_μ= 2.5 is used to attach flow and generate a super-lift coefficient. The angle of attack is 65° for the CFJ airfoil, and 14° for the baseline airfoil.

2.7 Boundary Conditions

Freestream total pressure, total temperature, and flow angle are specified along the upstream portion of the far field boundary. The freestream static pressure is specified along the downstream far field boundary to create the intended freestream Mach number. A periodic boundary condition is applied in the spanwise direction. The adiabatic non-slip wall treatment suggested in [32] is used to achieve flux conservation by shifting a half interval of the mesh on the wall. If the wall surface normal direction is in η-direction, the no slip condition is enforced on the surface by computing the wall inviscid flux $F_{1/2}$ in the following manner. Third-order interpolation is used at the wall.

$$\mathbf{F_w} = \begin{pmatrix} \rho V \\ \rho u V + p\eta_x \\ \rho v V + p\eta_y \\ \rho w V + p\eta_z \\ (\rho e + p)V \end{pmatrix}_w = \begin{pmatrix} 0 \\ p\eta_x \\ p\eta_y \\ p\eta_z \\ 0 \end{pmatrix}_w \tag{38}$$

2.7.1 C_μ Iteration

To achieve zero net mass flux with the CFJ flow control, the mass flow exiting the injection slot must be equal to the mass flow entering the suction slot, i.e. $\dot{m}_{inj} = \dot{m}_{suc}$. The prescribed jet momentum coefficient C_μ is achieved by iteratively adjusting the injection cavity total pressure. The injection and suction mass flow rates are matched by then adjusting the suction cavity static pressure. The total temperature increment is assumed constant in this study. This iterative process is conducted throughout the simulation until the specified momentum coefficient is reached and the injection and suction mass flow match the setpoint within an acceptable tolerance, which is $\epsilon = 0.5\%$ for the present study.

3 Results and Discussion

3.1 Aerodynamic Performance

Fig. 5 shows the mid-plane instantaneous Mach contours (left) and time averaged Mach contours (right) of the CFJ6421 airfoil at $\alpha = 65°$. The flow is well attached. The time-averaged flow field structure of the 3D IDDES CFJ airfoil is similar to that of the 2D URANS airfoil at similar conditions, showing a super-suction region above the leading edge, a stagnation region below the trailing edge, and attached flow along the entire surface [1]. Like the 2D flow field, the 3D flow field shows that the leading edge stagnation point is positioned on the airfoil pressure surface very near the trailing edge. The 2D study of this airfoil showed that once C_L exceeds 13.7, a new detached stagnation point forms in the region below the airfoil, forming a high pressure circulating region [1]. Consistent with the 2D study, the circulation of the flow around this 3D airfoil is not sufficient to form the detached stagnation point below the airfoil. The CFJ airfoil has a significant influence on the flow field. As the far field flow approaches the airfoil, a large volume is deflected upwards and around the airfoil. The near field flow first approaches the tail of the airfoil, then travels up the pressure surface, accelerating around the leading edge and mixing with the injection jet flow before travelling down the suction surface, eventually returning to the main flow. At the leading edge of the CFJ airfoil, the peak Mach number reaches 0.615, 9.8 times higher than the freestream Mach number. This accelerated flow generates a "super-suction" effect at the leading edge that contributes to the super-lift coefficient and thrust generation. This Co-Flow Jet simulation shows a reversed wake velocity deficit, consistent with other CFJ studies [40, 10].

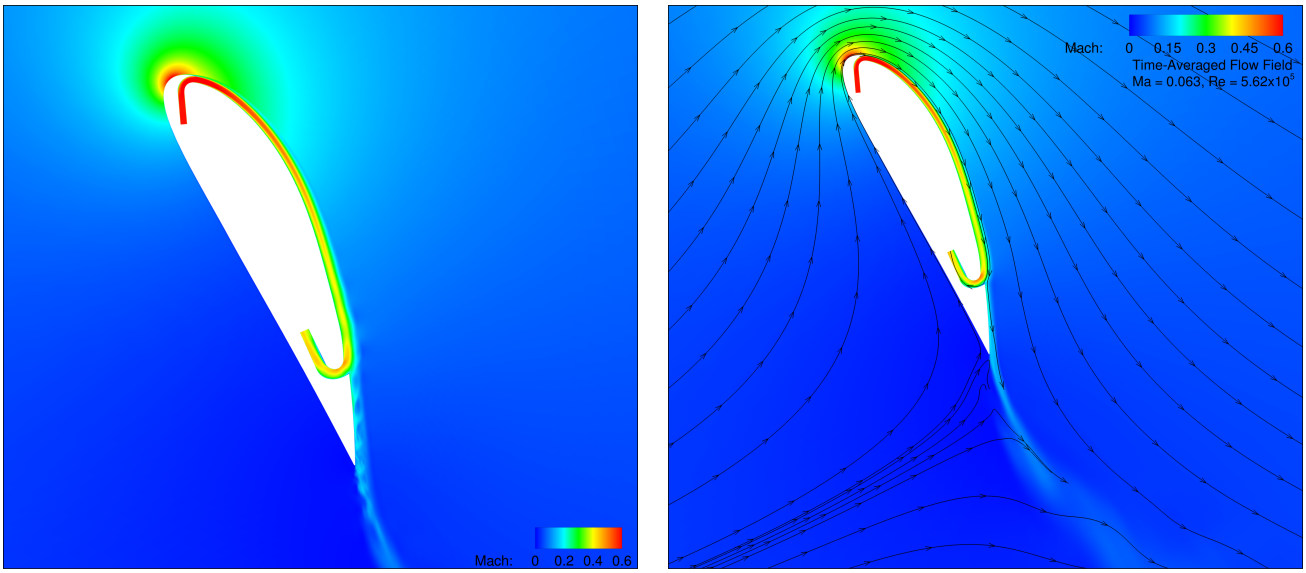

Figure 5: Instantaneous (left) and time averaged (right) flow fields around the CFJ airfoil.

Figures 6 and 7 illustrate the vortex structures created by the CFJ airfoil using a Q-criterion isosurface at Q=1.0, which highlights regions of the flow field dominated by vorticity. The isosurface is colored by vorticity magnitude. The flow on the pressure surface, around the leading edge, and in the region around the injection jet is stable. The greatest EAPG occurs immediately after the injection duct, but the flow remains well attached. This is due to the injection jet energizing the boundary layer, primarily through turbulent eddy viscosity diffusion [1, 41]. A strong shear layer forms between the fast moving wall jet and the comparatively slower moving outer flow. Downstream of the injection jet, around 50% of the airfoil chord, this shear layer devolves into a shear layer instability, forming conjugate pairs of spanwise vortices. This shear layer instability is shown by the spanwise

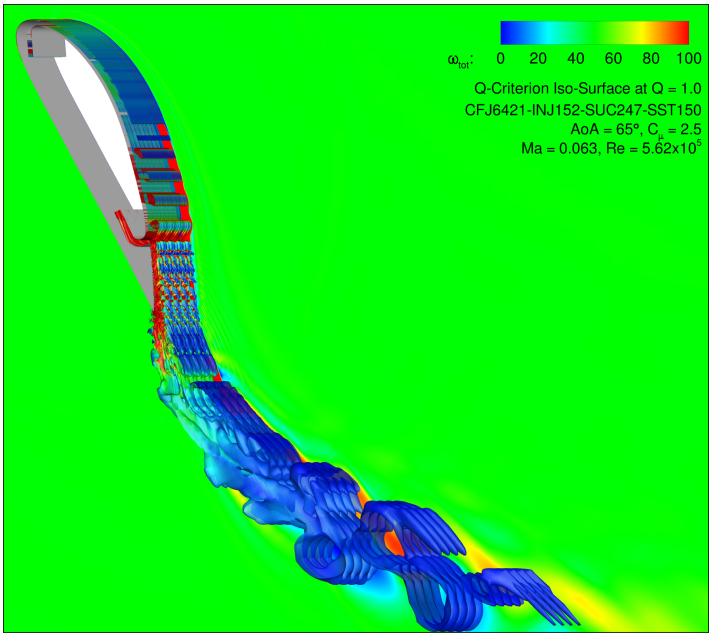

Figure 6: CFJ airfoil vortex shedding.

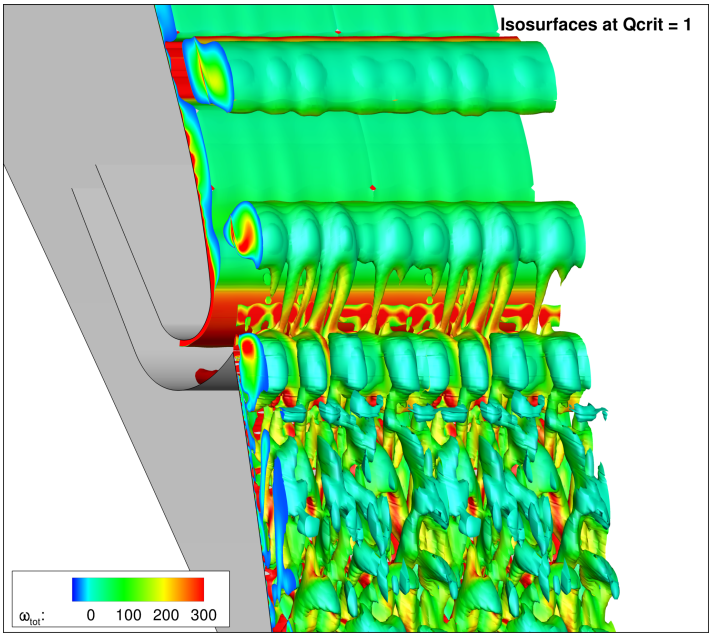

Figure 7: CFJ airfoil vortices over suction duct.

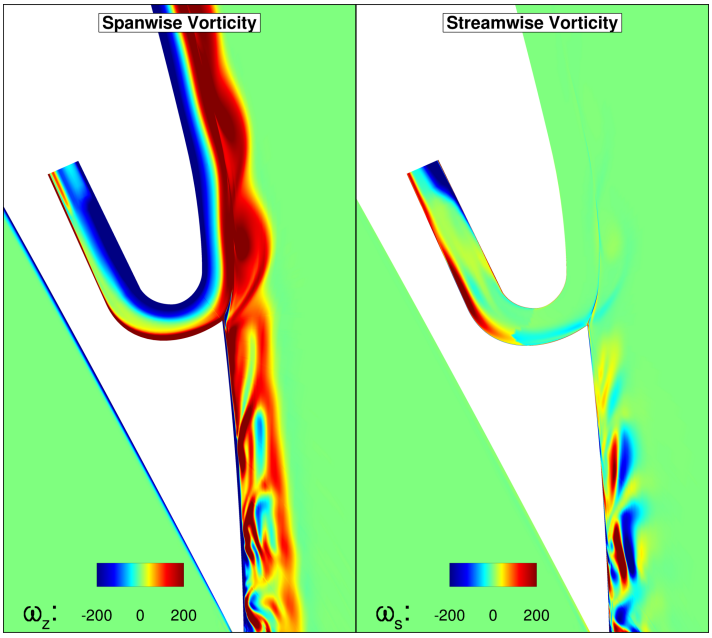

Figure 8: CFJ suction region spanwise and streamwise vortex magnitude comparison.

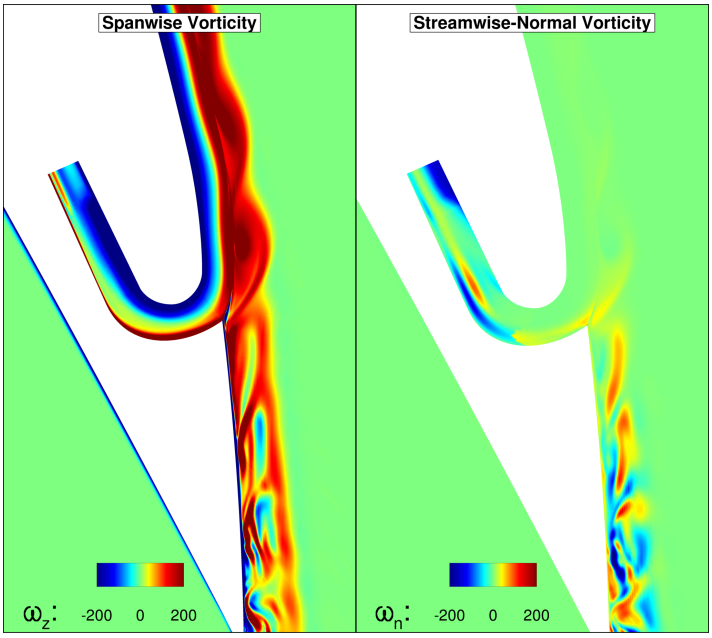

Figure 9: CFJ suction region spanwise and normal vortex magnitude comparison.

vortex tubes "rolling" down the aft of the airfoil. The low pressure vortex cores move along the airfoil surface, causing local pressures to rise and fall periodically. Fig. 12 is a Fourier transform a nodal pressure signal. A single point was selected on the z-midplane of the domain, 2%C vertically above the suction inlet lip. The core of the spanwise vortex tubes pass through this point. The static pressure was recorded in each time step. The dominant reduced frequency of this pressure oscillation in the shear layer is found to be $\bar{f} = 37.44 \pm 0.41$. The lower energy peaks are harmonics of the dominant frequency. These harmonics are most likely numerical artifacts from the FFT algorithm, but could be related to other unsteady interactions or aeroacoustic noise from pressure waves reflecting from the airfoil surfaces.

The sharp lip of the suction duct inlet appears to split the clockwise and anticlockwise regions of the spanwise vorticity field, diverting the inner clockwise layer into the suction duct, and allowing the outer anticlockwise layer to pass the suction lip. Without its conjugate, the anticlockwise-spanwise vorticity layer rapidly decomposes into streamwise and transverse vortex elements. Figures 8 and 9 clearly show that upstream of the suction lip, the flow has essentially no streamwise or transverse vorticity components, but downstream of the suction inlet lip these two vorticity components become much more significant. While the vorticity downstream of the suction slot is remains spanwise-vortex dominant, the other components grow to a similar order of magnitude. The mechanism driving this transformation of the vortices after the suction lip is uncertain, and merits further study. While the vorticity is significantly more isotropic after the suction inlet lip, it is important to note that the flow in this region is still characterized by coherent vortex structures. The unsteady wake flows smoothly down the tail surface in organized structures, undulating in a wave-like progression. Figures 10 and 11 show a snapshot of these structures. Figure 10 shows instantaneous mid-plane flow fields of the density and Mach number, while Fig. 11 shows iso-surfaces of the density, colored by velocity. The flow actually moves much more rapidly in a narrow band close to the surface of the airfoil. An animation of this effect is available at (https://youtu.be/Ysne9vUZFSU). The streamwise and transverse vortex structures may be beneficial, enhancing the wake mixing near the airfoil's trailing edge and generating a shallower wake profile than conventional airfoils.

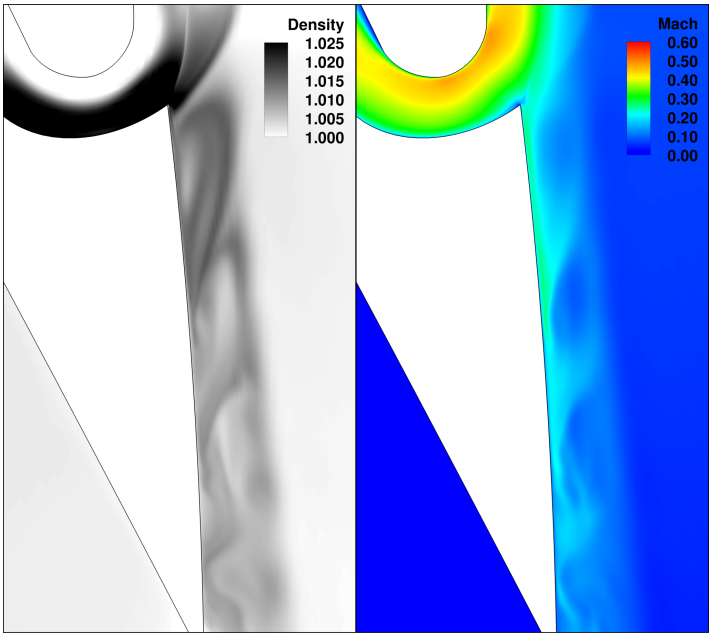

Figure 10: Mach and density contours after CFJ suction.

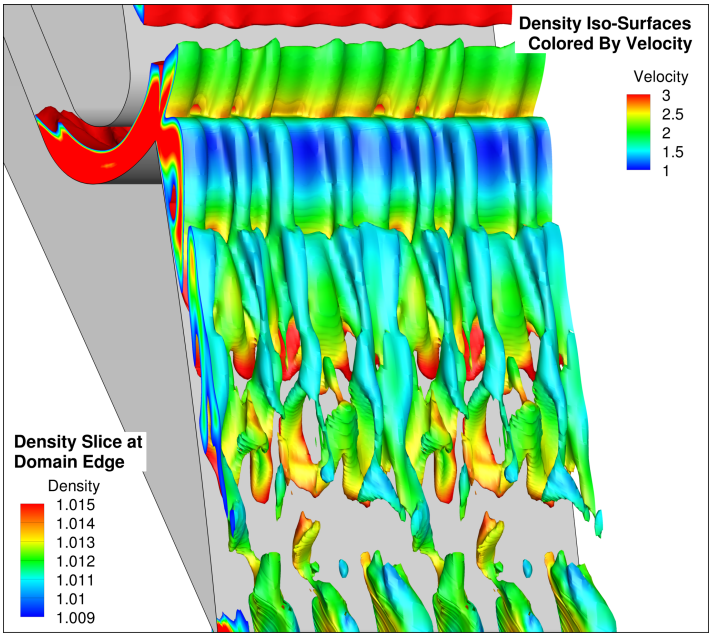

Figure 11: Density isosurfaces after CFJ suction.

Table 2: Performance of CFJ and Baseline Airfoils

Case	C_μ	C_L	C_D	P_C	C_L/C_D	C_L/C_{Dc}	Γ	$PG_{x\ max}$	$PG_{r\ max}$
Baseline	N/A	1.514	0.105	N/A	14.433	14.433	N/A	3.19	9.27
CFJ	2.50	9.583	0.028	3.539	343.305	2.687	1.076	4715	5571

Figures 13a and 13b show the total lift and drag forces oscillating in time with a reduced frequency $\bar{f} = 37.04$. This corresponds to the instability frequency of the jet shear layer, from Fig. 12. The lift coefficient oscillates by about $\pm 1\%$ of its mean value. While the pressure in the injection jet is very steady, the pressure in the suction jet rises and falls as the shear layer vortices interact with the suction slot. Thus the pressure ratio between the injection and suction ducts varies, resulting in an oscillating power required, shown in Figs. 13c and 13d.

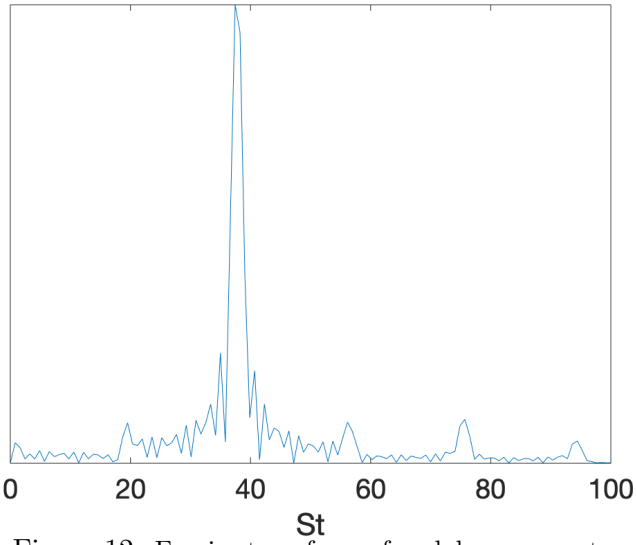

Figure 12: Fourier transform of nodal pressure at a position 2%C vertically above suction inlet lip.

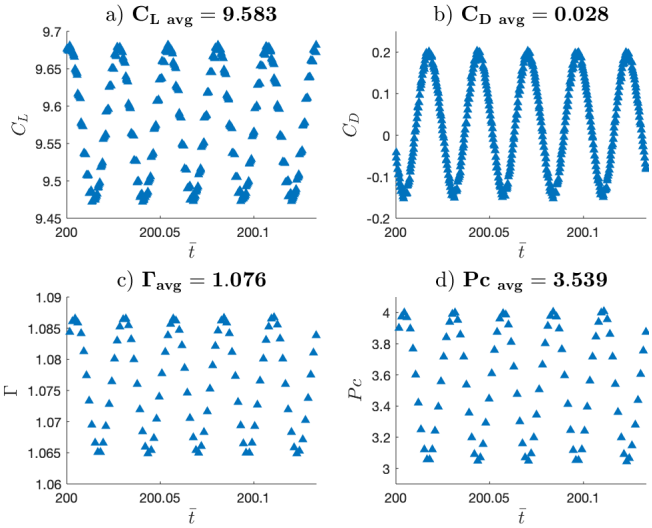

Figure 13: CFJ airfoil aerodynamic coefficients for lift, drag, pressure ratio, and power required in time.

The accelerated flow around the LE and suction surface of the CFJ airfoil in conjunction with the high pressure stagnation region below the airfoil produces a strong net lifting force. The substantial lift created by the CFJ airfoil is not attributed to the jet reaction force. Referring to Eqns. 34–37, the pressure and momentum terms of the jet are actually a detriment to the total lift, due to the nearly horizontal injection jet direction and near vertical suction jet direction. The pressure on the airfoil's surface periodically oscillates due to the unsteady nature of the flow. The surface force R'_y oscillates as 15.12 ± 0.105, while the jet force F_{ycfj} oscillates as -5.54 ± 0.089. Although the injection and suction jets seem to produce negative lift, they provide the means to establish the attached flow field that generates super-circulation and the super-lift coefficient. The injection jet does produce a positive horizontal force, at times overcoming the drag on the airfoil to produce a net thrust. Table 2 shows the computed time-averaged aerodynamic coefficients for the 3D IDDES CFJ6421 airfoil.

Fig. 14 shows the computed time-averaged midplane airfoil surface pressure coefficient $-C_p$ for the CFJ airfoil at 65° AoA and $C_\mu = 2.5$ (left) and the baseline airfoil at its peak C_L at 14° AoA (right). The baseline airfoil has a suction peak $-C_p$ of almost 2.7, whereas the CFJ-NACA6421 airfoil's suction peak value is close to 86, about 32 times higher than the baseline. This greater suction peak is of course caused by the accelerated flow around the leading edge, creating a super suction effect.

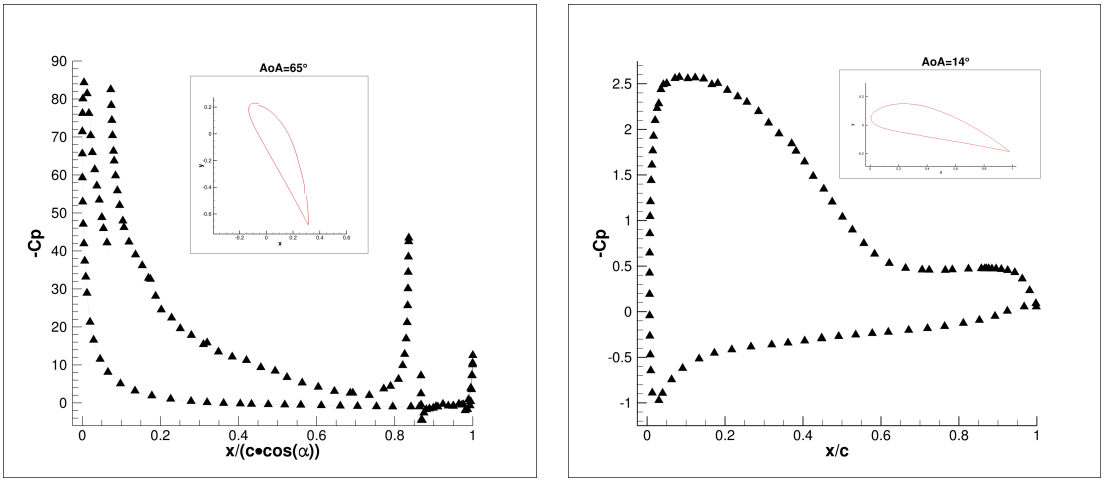

Figure 14: C_p plots for CFJ airfoil (left), and baseline airfoil (right).

3.2 Pressure Gradients

Per the definition of an EAPG, the CFJ airfoil is compared to a baseline NACA6421 airfoil at its $C_{L\ max}$ condition. A 2D URANS angle of attack study at Mach = 0.063 and Re = 5.62×10^5 determines that $C_{L\ max}$ = 1.511 for the baseline NACA6421 airfoil occurs at $AoA = 14°$. The 3D NACA6421 airfoil is simulated using IDDES at the same flow conditions and 14° angle of attack. Table 3 shows that the time-averaged lift coefficient and pressure gradients are nearly identical between the 2D URANS and 3D IDDES results. Thus the 2D URANS stall AoA of 14° is adopted as the 3D IDDES stall AoA to save simulation time. This assumption may not be perfect, but it is believed to be acceptable not just by the quantitative results in Table3, but also by the qualitative results shown in Figs. 15 and 16, which show very similar flow fields. These instantaneous Mach contours of the 2D URANS and the 3D IDDES mid-plane denote the location and magnitude of the maximum streamwise and radial pressure gradients. Both simulations of the baseline NACA6421 airfoil show flow separation starting at about 54% x/c, on the suction surface. The maximum streamwise pressure gradient is located at the flow separation inception point. The maximum radial pressure gradient is located near the leading edge. Figures 17 and 18 further show the flow structures of the 3D IDDES baseline airfoil using Q-criterion isosurfaces colored by the total vorticity.

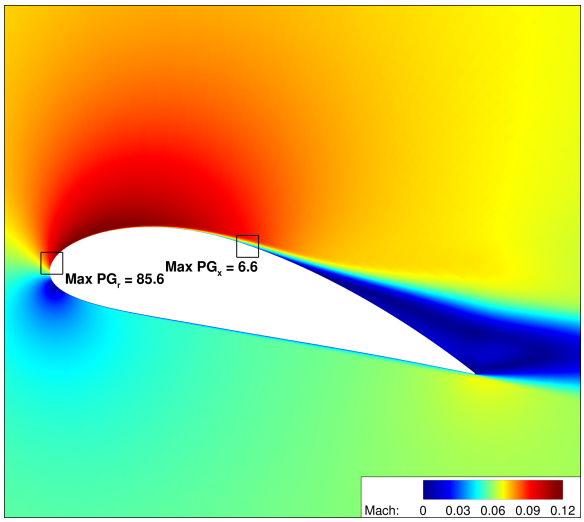

Figure 15: 2D URANS Mach contour.

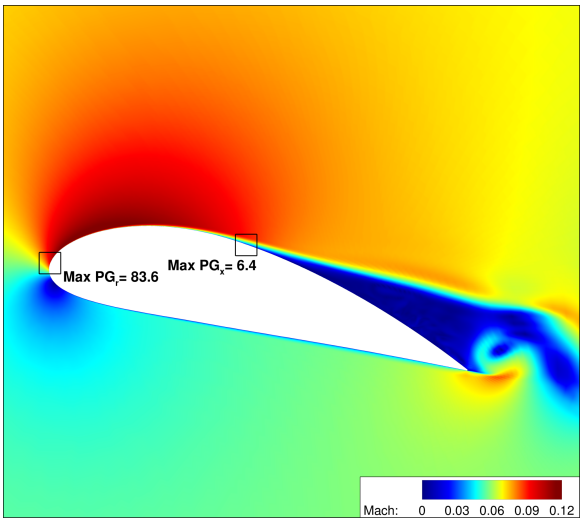

Figure 16: 3D IDDES midplane Mach contour.

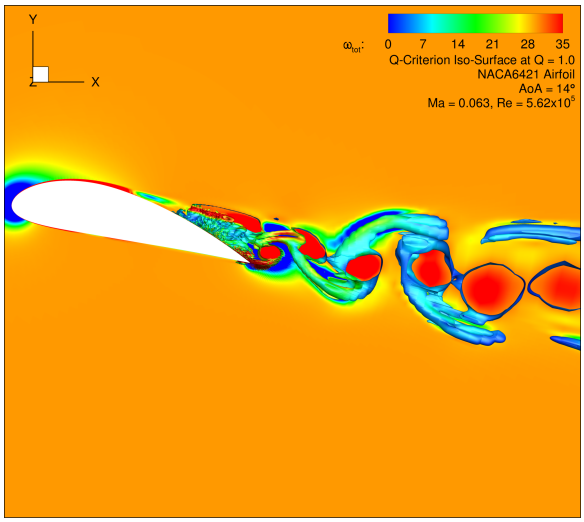

Figure 17: 3D IDDES midplane vorticity magnitude contour with Q isosurface.

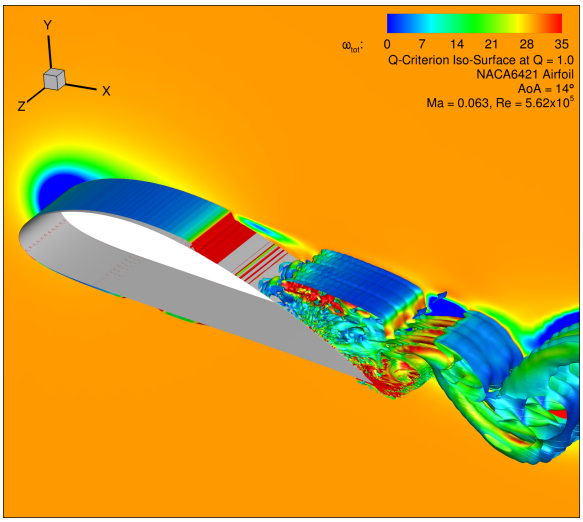

Figure 18: 3D IDDES perspective vorticity magnitude contour with Q isosurface.

Table 3: Pressure Gradients of 2D and 3D CFJ Airfoils

Case	C_μ	C_L	$PG_{x\ max}$	$PG_{r\ max}$	PGR_x	PGR_r
2D Baseline	N/A	1.511	6.6	85.6	-	-
2D CFJ	1.70	9.662	1502	947	223	11.1
3D Baseline	N/A	1.514	6.4	83.6	-	-
3D CFJ	2.50	9.583	4714	5663	737	67.7

The 3D CFJ airfoil demonstrates the ability create and sustain an EAPG around the leading edge and down the length of the suction surface. It accomplishes this via the energy and momentum transfer of the CFJ, effectively controlling the external flow to overcoming the extreme adverse pressure gradient and maintain attached flow. If the flow detaches, the APG is relaxed. The CFJ airfoil is able to boost the APG to magnitudes far greater than the baseline airfoil would be able to sustain.

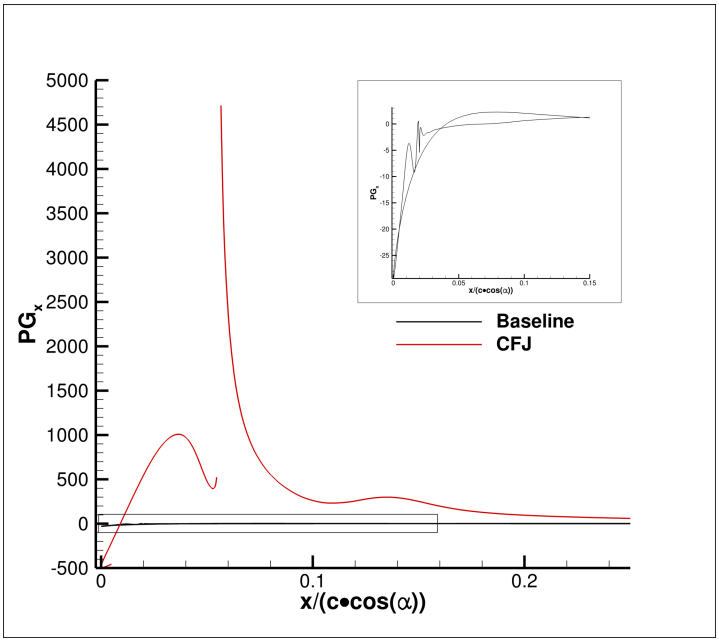

Figure 19: 3D CFJ airfoil streamwise pressure gradient distribution.

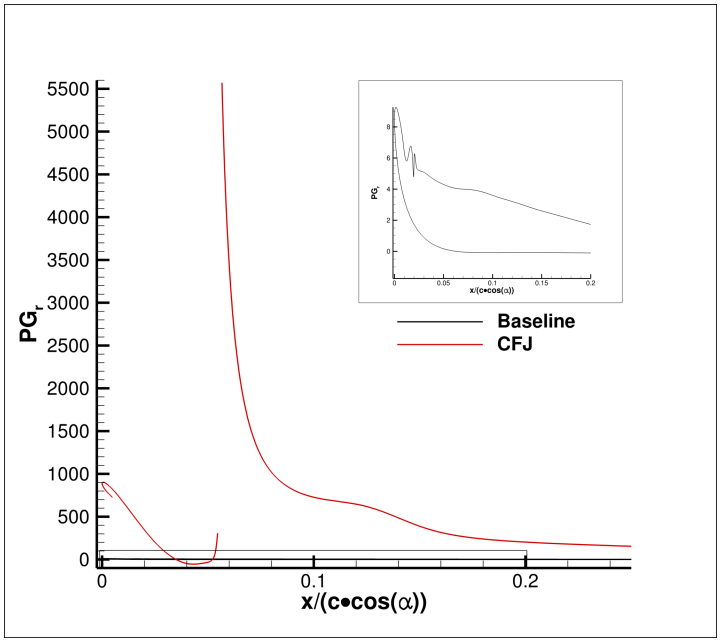

Figure 20: 3D CFJ airfoil radial pressure gradient distribution.

Fig. 19 shows that at the very leading edge of the airfoil, the flow experiences a favorable streamwise pressure gradient, but it quickly rises to an adverse pressure gradient past the leading edge. The PG_x reaches 1008, 158 times greater than the baseline, qualifying the APG of the CFJ airfoil an an EAPG. This EAPG declines somewhat approaching the injection slot. The global maximum streamwise pressure gradient coefficient PG_x occurs at the injection jet, with a value of $PG_x = 4714$, 737 times greater than the baseline, as listed by PGR_x in Table 3. The EAPG decreases rapidly downstream of the injection slot, but maintains an EAPG two or three orders of magnitude higher than the baseline until the suction slot. Fig. 20 shows that the radial adverse pressure gradient increases in strength as the flow moves towards the airfoil's leading edge, peaking at $PG_x = 903$, 10.8 times greater than the baseline's $PG_x = 83.6$. It then decreases in strength past the leading edge before rising again at the injection slot lip. The maximum PG_r for the CFJ airfoil is measured at injection slot, with a value of $PG_r = 5663$, 68 times higher than the baseline, as listed by PGR_r in Table 3. The time-averaged pressure field and positions of each maximum pressure gradient coefficient can be seen in Fig. 21.

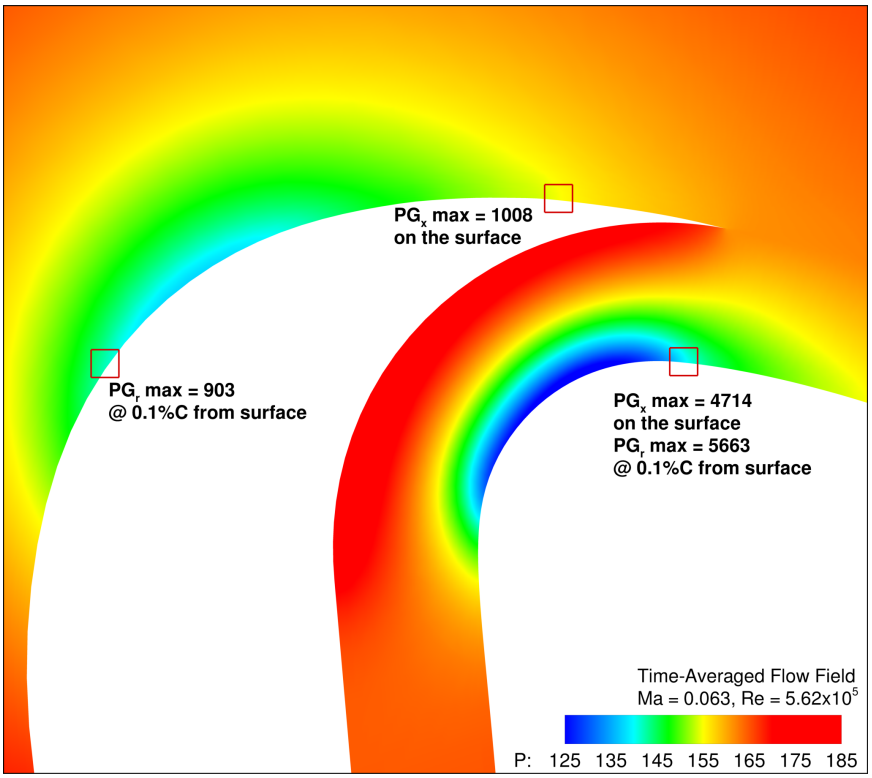

Figure 21: CFJ pressure gradient maximums, showing points at leading edge and injection slot.

The PG_r close to the wall is heavily influenced by the local radius of curvature of the wall, especially inside the injection duct. Inside the injection duct the minimum radius of curvature is just 1.8%C, about half the radius of curvature of the airfoil leading edge, which has a radius of curvature of 3.8%C. The PG_r term from Eq. 1 is proportional to the radius of curvature, thus the radial pressure gradients observed inside the injection duct are higher than those around the LE of the airfoil. The injection duct itself is a necessary construction used to implement the C_μ control, to turn the flow from the modeled compressor actuator to the injection slot. This paper does not evaluate the pressure gradients within the injection and suction ducts. Table 4 lists the magnitude of each APG maximum for the leading edge and for the injection slot.

Table 4: Maximum Pressure Gradients of Studied Airfoils

Case	C_μ	C_L	$LE\ PG_{x\ max}$	$LE\ PG_{r\ max}$	$INJ\ PG_{x\ max}$	$INJ\ PG_{r\ max}$
2D Baseline	N/A	1.511	6.6	85.6	N/A	N/A
3D Baseline	N/A	1.514	6.4	83.6	N/A	N/A
3D CFJ	2.50	9.583	1008	903	4714	5663

3.3 Flow Attachment Evaluated Using Turbulent Wall Jet Momentum Equation

3.3.1 Wall Jet Momentum Equation and Attachment Criteria

The turbulent wall jet momentum equation is used to evaluate the flow attachment on the surface. This method is previously used to evaluate the flow of the 2D CFJ airfoil [41]. This method is adopted to more thoroughly understand the EAPG flow simulated by 3D IDDES. We use the wall jet momentum equation in its 2D form, assuming that we have plane flows in the regions we evaluate. While this wall jet momentum equation is derived for low curvature geometry [**?**], analysis with high curvature in [41] shows the dominant terms of the wall jet equation are the same. We use this approach to estimate the contribution of each term to maintaining flow attachment. In the below equations, x refers to the local streamwise direction tangent to the wall surface, and y is the direction normal to the wall surface. The viscosity μ is composed of the molecular viscosity and turbulent eddy viscosity. The turbulent wall jet momentum equation in x direction can be written in non-dimensional, partial difference form as the following [17]:

$$\rho u\frac{\partial u}{\partial x}+\rho v\frac{\partial u}{\partial y}-\frac{1}{Re}\frac{\partial \mu}{\partial y}\frac{\partial u}{\partial y}+\frac{\partial p}{\partial x}=\frac{1}{Re}\mu\frac{\partial^2 u}{\partial y^2} \tag{39}$$

A more general criterion for separation control is suggested by Xu et al. [17]. This separation criteria is valid for laminar and turbulent flows. They state that is is more energy efficient to seek "attached elevated flows" with adverse pressure gradients instead of attached flows with favorable pressure gradients. The attached velocity profiles will have $\tau_w > 0$ $(\partial u/\partial y > 0,\ \omega_z < 0)$ with $[\partial^2 u/\partial y^2]_w \geq 0$. The $[\partial^2 u/\partial y^2]_w = 0$ case includes zero pressure gradient situations. If $\partial u/\partial y < 0$, the flow is separated [17].

An APG *can* be overcome along a wall by the flow's momentum convection and turbulence diffusion. The first two terms on the LHS of Eq. 39 are the convective terms, which are responsible for transferring the wall jet momentum in the streamwise and transverse flow directions. In the wall jet, these two terms are similar in magnitude due to the high velocity gradient imposed by the CFJ injection [17]. The third term is the momentum diffusion due to the turbulent eddy viscosity gradient. This term is negligible for laminar flow since the viscosity is fairly constant, but is dominant for the turbulent mixing due to the tremendous growth rate of turbulent eddy viscosity near the wall for the CFJ [41]. This turbulent diffusion is of particular importance to maintaining attached flow in an EAPG. All of the first three terms on the LHS of Eq. 39 are responsible for offsetting the APG, however the diffusion term plays the most significant role in transferring momentum inward to energize the boundary layer, and outward to entrain the main flow.

The velocity gradient at the wall can be expressed in terms of spanwise vorticity, with the substitution:

$$\omega_z=\frac{\partial v}{\partial x}-\frac{\partial u}{\partial y}\approx-\frac{\partial u}{\partial y} \tag{40}$$

An injection wall jet tangent to the wall surface has $\frac{\partial v}{\partial x} << \frac{\partial u}{\partial y}$ except in the region close to the suction slot entrance. The wall jet momentum Eq. 39 may then be rewritten as:

$$\rho u\frac{\partial u}{\partial x}-\rho v\omega_z+\frac{\omega_z}{Re}\frac{\partial \mu}{\partial y}+\frac{\partial p}{\partial x}=\frac{\mu}{Re}\frac{\partial^2 u}{\partial y^2} \tag{41}$$

The strong spanwise vorticity flux along the CFJ's injection duct surfaces play a crucial role in attaching the wall jet flow in the presence of an EAPG.

3.3.2 Evaluation of Turbulent Wall Jet Momentum Equation Terms

Four positions of interest are selected in the mid-plane to visualize the flow attachment term distributions, shown in Figs. 22–23. Position A is the leading edge of the airfoil. Position B is located 1%C upstream of the injection slot. Position C is 1%C downstream of injection jet. Position D is 20%C downstream of the injection jet.

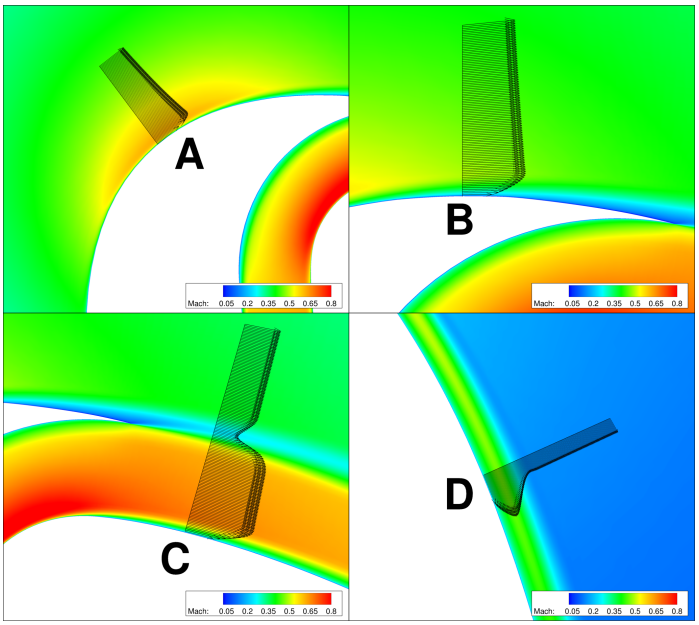

Figure 22: Positions for evaluating flow attachment.

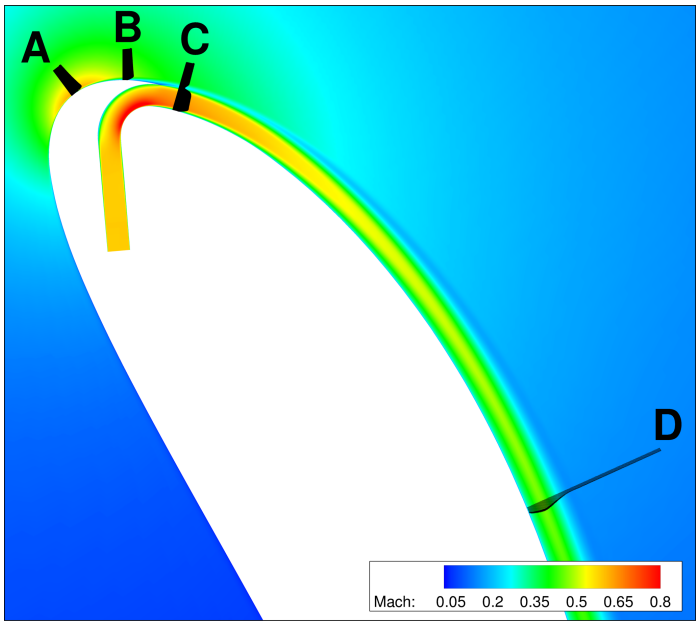

Figure 23: Positions for evaluating flow attachment.

Figures 24–27 plot the turbulent wall jet momentum equation terms for each point. The vertical axis is y^+, the dimensionless wall distance. y^+ values up to about 5 are in the viscous sublayer. y^+ values of about 5–30 are the buffer layer. y^+ values of about 30–1000 correspond to the inertial boundary layer. These plots have a maximum y^+ of 100, so they focus on a region very close to the wall, about $1/10^{th}$ the thickness of the boundary layer.

At position A, the leading edge of the airfoil, the flow is in a favorable pressure gradient. The sum of the LHS of Eq. 39 is negative everywhere, and the flow is attached.

At position B, 1%C upstream of the injection jet, the adverse pressure gradient (cyan line) comes into play, working against the other terms. The LHS sum of Eq. 39 is positive on the wall (black line). The turbulence diffusion term (yellow line) grows rapidly above the viscous sublayer. Joined by the much smaller streamwise inertial force term, $\rho u \cdot \partial u/\partial x$ (blue line), they overwhelm the EAPG within the boundary layer, moving the sum of the LHS to be negative off the wall. The turbulent eddy viscosity diffusion, $\frac{1}{Re}\frac{\partial \mu}{\partial y}\frac{\partial u}{\partial y}$, plays a major role in the flow attachment around the LE of the airfoil.

At position C, 1%C downstream of the injection jet, the EAPG (cyan) is substantially greater than the APG of position B. The spanwise vorticity ω_z is also highest here due to the strong vorticity flux on the inner duct walls of the injection jet. The turbulent eddy viscosity diffusion is exceptionally large, reaching a magnitude five times greater than the turbulence diffusion at position B. The turbulent eddy viscosity diffusion term greatly exceeds the EAPG and maintains a negative LHS sum off of the wall.

At position D, 20%C downstream of the injection jet, the turbulent eddy viscosity diffusion term tapers in strength by about half compared to position C, but remains high. The adverse pressure gradient also reduces in strength about 90%. The turbulence diffusion term again overcomes the APG and maintains flow attachment.

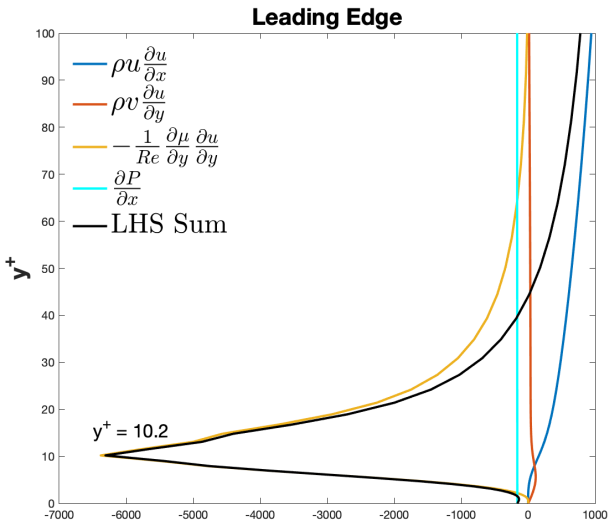

Figure 24: Position A.

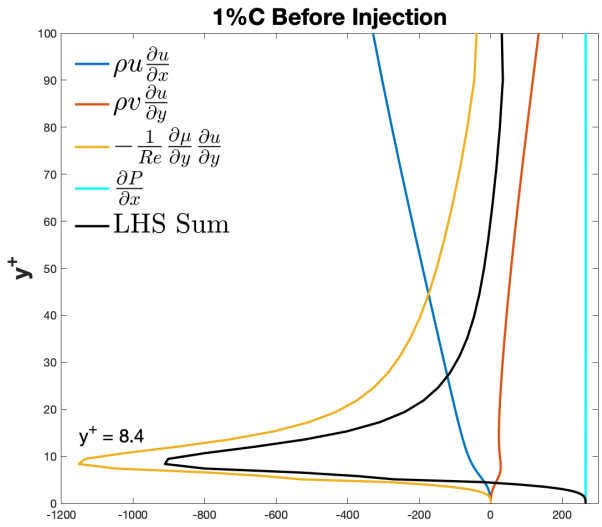

Figure 25: Position B.

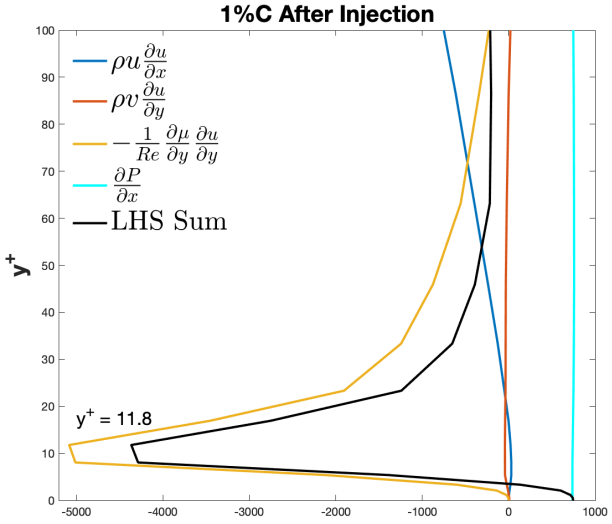

Figure 26: Position C.

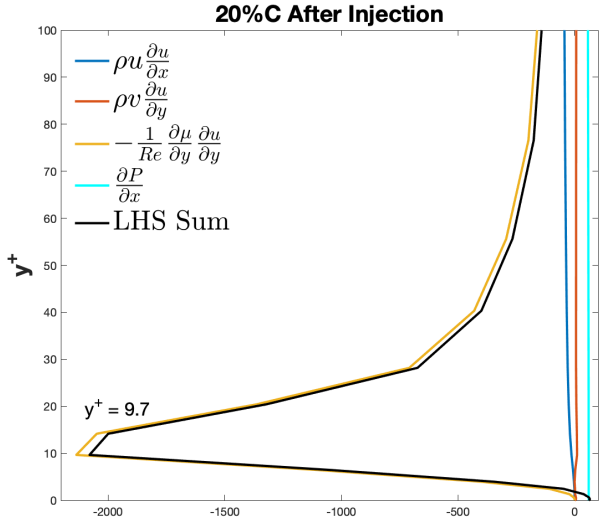

Figure 27: Position D.

Looking at Figs. 24–27, it is clear that for the CFJ in an EAPG, the turbulent eddy viscosity diffusion term is overwhelmingly responsible for energizing the boundary layer to sufficiently overcome the adverse pressure gradient. This term is also most responsible for transporting momentum and energy from the CFJ injection jet to the adjacent main flow, influencing attachment upstream of the injection jet as well as downstream.

The turbulent eddy viscosity diffusion term is made up of two factors. The first term is $\partial\mu/\partial y$, the turbulent viscosity gradient. As mentioned previously, the viscosity is made up of the molecular viscosity and the turbulence eddy viscosity. The molecular viscosity only changes small amounts with variation in temperature. It is the eddy viscosity that varies significantly in this study. The narrow CFJ injection jet has an incredibly high velocity gradient near the wall, creating a very sharp turbulent eddy viscosity gradient. Figure 28 compares the molecular viscosity to the turbulent eddy viscosity at position C, and plots them against their gradient, $\partial\mu/\partial y$. The horizontal axis is the orthogonal distance from the wall (D) normalized by the injection slot height (H), which is 1.52% of

the airfoil chord length. D/H = 1 is the outer wall of the injection slot. The molecular viscosity varies very little compared to the other terms. The turbulent eddy viscosity spikes to about 50 times the molecular viscosity in the inner boundary layer, and 80 times the molecular viscosity in the outer boundary layer. It is nearly zero in the center of the jet where the velocity profile is fairly uniform. The largest viscosity gradient occurs in the buffer layer, with a value of about 1.4×10^5.

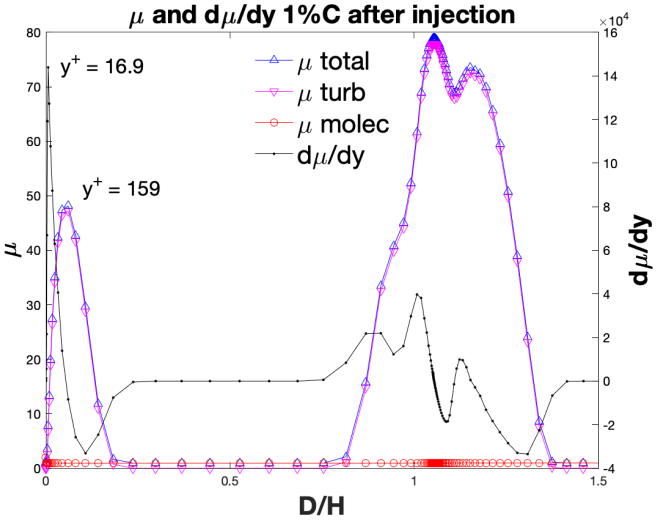

Figure 28: Viscosity components and viscosity gradient across the CFJ injection jet. Point C.

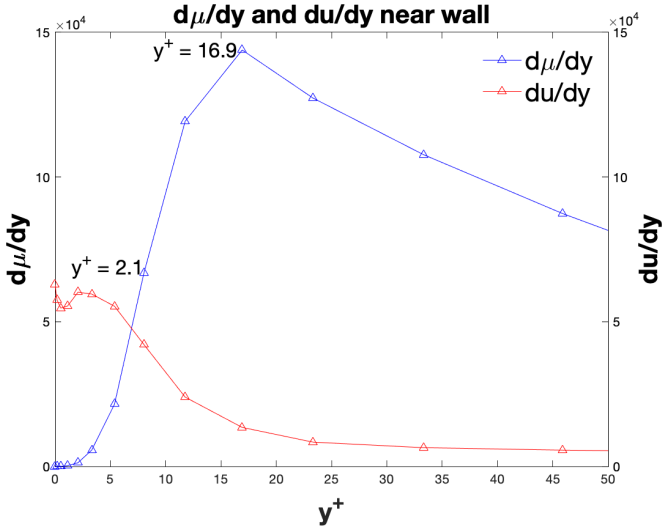

Figure 29: Velocity and viscosity gradients withing the inner boundary layer. Point C.

The second component of the turbulent eddy viscosity diffusion term is the velocity gradient, $\partial u/\partial y$. On the wall, this term approximates the spanwise vorticity. The velocity rapidly grows from zero on the wall to Mach 0.85 in a distance of less than 15% of the injection slot height. The enforcement of a smooth, non-slip, adiabatic wall boundary condition forces the velocity gradient $\partial u/\partial y$ to be very high. Figure 29 shows the non-dimensional velocity gradient to be about 6×10^4 near the wall. Figure 29 also shows how the velocity gradient is the most significant factor within the laminar viscous sublayer, but in the inner layers of the boundary layer, the viscosity gradient is dominant.

This analysis of the CFJ in an EAPG shows that a strong vortex flux on the wall enables the turbulent eddy viscosity diffusion to transfer energy from the injection jet down to the innermost layers of the boundary layer, energizing the flow to overcome the extreme adverse pressure gradient. The eddy viscosity gradient facilities the transfer of energy and momentum from the jet down through the boundary layer, but also out to the surrounding flow. It is this exceptional momentum and energy transfer which enables to CFJ active flow control system to so effectively influence the domain around the airfoil.

4 Conclusions

This paper conducts a 3D Improved Delayed Detached Eddy Simulation, verifying the findings of our previous 2D URANS study. The Co-Flow Jet active flow control airfoil is numerically shown to sustain flows with Extreme Adverse Pressure Gradients. This paper simulates the flow around a CFJ6421-SST150-SUC247-INJ152 airfoil at an angle of attack of 65° and a jet momentum coefficient (C_μ) of 2.5, which achieves a super-lift coefficient of $C_L = 9.58$. The baseline NACA6421 airfoil is also simulated using IDDES at an AoA of 14°, at its $C_{L_{max}}$ condition, just before stalling.

The CFJ airfoil demonstrates a remarkable ability to maintain attached flow at $\alpha = 65°$, generating an EAPG around the leading edge of the airfoil and downstream of the injection slot. The CFJ airfoil sustains maximum streamwise and centrifugal pressure gradient coefficients of 4714 and 5663 respectively, whereas the baseline airfoil with no flow control achieves the corresponding maximum values of 6.4 and 83.6. The CFJ thus augments the streamwise and centrifugal pressure gradients by 737 times and 68 times, respectively. The turbulent diffusion is found to play a dominant role to offset the EAPG and make the flow attached.

In this research, the CFJ pumping efficiency is set to 100% to calculate the nominal power required to drive the injection jet flow and achieve the desired influence on the greater flow field. The actual power depends on the pumping efficiency as indicated by Eq. 31. The pumping efficiency would vary for different actuators. The Co-Flow Jet micro-compressor actuators used in previous studies can achieve a very good efficiency of 80% and above [42, 13, 43, 44]. A lower power required coefficient is essential for an AFC method to be efficient and effective. If an AFC method has a high power requirement to be effective, it is unlikely to benefit the system as a whole. Co-Flow Jet AFC demonstrates both high effectiveness and high efficiency [15]. The power required is also a parameter that can be accurately measured in a laboratory and via simulation for a ZNMF flow control system. The companion paper to this study investigates the effect on the CFJ airfoil system when using a 70% efficient pump. This setup has an injection flow with higher total enthalpy due to entropy losses, and better reflects a real Co-Flow Jet system with system energy losses and hot injection flow [45].

In conclusion, this research represents a significant step forward in the understanding and application of the CFJ technology. The insights gained from the use of IDDES in simulating EAPG-CFJ interactions offer a solid foundation for future explorations in this field. Continued investigation and development are essential to fully realize the potential of the CFJ technology in promoting aerodynamic performance across various sectors.

5 Acknowledgments

The simulations are conducted on Pegasus super-computing system at the Center for Computational Sciences at the University of Miami.

Disclosure: The University of Miami and Dr. Gecheng Zha may receive royalties for future commercialization of the intellectual property used in this study. The University of Miami is also equity owner in CoFlow Jet, LLC, licensee of the intellectual property used in this study.

References

[1] McBreen, B., Xu, K.-W., and Zha, G.-C., "Numerical Study of Extreme Adverse Pressure Gradients Enabled by Co-Flow Jet," AIAA Paper 2023-1430, AIAA SciTech Forum, National Harbor, MD, 23-27 January, 2023.

[2] Yang, Y.-C. and Zha, G.-C., "Super-Lift Coefficient of Active Flow Control Airfoil: What Is the Limit?" AIAA Paper 2017-1693, AIAA SCITECH2017, 55th AIAA Aerospace Science Meeting, Grapevine, Texas, 9-13 January 2017.

[3] Zha, G.-C. and Gao, W. and Paxton, C., "Jet Effects on Co-Flow Jet Airfoil Performance," *AIAA Journal, No. 6,*, Vol. 45, 2007, pp. 1222–1231.

[4] Zha, G.-C. and Paxton, D. C., "A Novel Flow Control Method for Airfoil Performance Enhancement Using Co-Flow Jet," *Applications of Circulation Control Technologies*, Chapter 10, p. 293-314, Vol. 214, Progress in Astronautics and Aeronautics, AIAA Book Series, Editors: Joslin, R. D. and Jones, G.S., 2006.

[5] Zha, G.-C and Paxton, C. and Conley, A. and Wells, A. and Carroll, B., "Effect of Injection Slot Size on High Performance Co-Flow Jet Airfoil," *AIAA Journal of Aircraft*, Vol. 43, 2006.

[6] Zha, G.-C and Carroll, B. and Paxton, C. and Conley, A. and Wells, A., "High Performance Airfoil with Co-Flow Jet Flow Control," *AIAA Journal*, Vol. 45, 2007.

[7] Wang, B.-Y. and Haddoukessouni, B. and Levy, J. and Zha, G.-C., "Numerical Investigations of Injection Slot Size Effect on the Performance of Co-Flow Jet Airfoil ," *AIAA Journal of Aircraft*, Vol. 45, 2008, pp. 2084–2091.

[8] Dano, B. P. E., Kirk, D., and Zha, G.-C., "Experimental Investigation of Jet Mixing Mechanism of Co- Flow Jet Airfoil," AIAA-2010-4421, (5th AIAA Flow Control Conference, Chicago, IL), 28 Jun - 1 Jul 2010.

[9] Dano, B. P. E., Zha, G.-C., and Castillo, M., "Experimental Study of Co-Flow Jet Airfoil Performance Enhancement Using Micro Discreet Jets," AIAA Paper 2011-0941, 49th AIAA Aerospace Sciences Meeting, Orlando, FL,, 4-7 January 2011.

[10] Lefebvre, A. and Dano, B. and Bartow, W. and Di Franzo, M. and Zha, G.-C., "Performance and Energy Expenditure of Co-Flow Jet Airfoil with Variation of Mach Number," *AIAA Journal of Aircraft*, Vol. 53, 2016, pp. 1757–1767.

[11] Wang, B. Y and Zha, G.-C., " Detached-Eddy Simulation of a Co-Flow Jet Airfoil at High Angle of Attack ," *AIAA Journal of Aircraft*, Vol. 48, 2011, pp. 1495–1502.

[12] Im, H.-S. and Zha, G.-C. and Dano, B. P. E., "Large Eddy Simulation of Coflow Jet Airfoil at High Angle of Attack," *Journal of Fluid Engineering*, Vol. 136(2), 2014, pp. 021101.

[13] Zha, G.-C., Yang, Y.-C., Ren, Y., and McBreen, B., "Super-Lift and Thrusting Airfoil of Coflow Jet-Actuated by Micro-Compressors," AIAA Paper 2018-3061, AIAA AVIATION 2018, Atlanta, GA , 25 - 29 June 2018.

[14] Xu, K.-W. and Zha, G.-C., "High Control Authority 3D Aircraft Control Surfaces Using Co-Flow Jet," *AIAA Journal of Aircraft*, July 2020.

[15] Xu, Kewei and Zha, Gecheng, "System energy benefit using co-flow jet active separation control for a serpentine duct," *Elsevier Journal of Aerospace Science and Technology*, Vol. 128, 2022, pp. DOI: 10.1016/j.ast.2022.107746.

[16] Xu, Kewei and Ren, Yan and Zha, Gecheng, "Numerical Analysis of Energy Expenditure for Co-Flow Wall Jet Separation Control ," *AIAA Journal*, Vol. 60, No. 5, 2022, pp. doi.org/10.2514/1.J061015.

[17] Xu, K.-W., Ren, Y., and Zha, G.-C., "Flow Separation Control by CoFlow Wall Jet," AIAA Paper 2021-2946, AIAA Aviation 2021, Aug. 2-6, 2021, 2-6 Aug. 2021.

[18] Smith, A., "High-Lift Aerodynamics," *Journal of Aircraft*, Vol. 12, 1975, pp. 501–530.

[19] Wang, Y., Yang, Y.-C., and Zha, G.-C., "Study of Super-Lift Coefficient of Co-Flow Jet Airfoil and Its Power Consumption," AIAA Paper 2019-3652, AIAA Aviation 2019, AIAA Applied Aerodynamics Conference, Dallas, Texas, 17-21 June 2019.

[20] Wang, Y. and Zha, G.-C., "Study of Mach Number Effect for 2D Co-Flow Jet Airfoil at Cruise Conditions," AIAA Paper 2019-3169, AIAA Aviation 2019, AIAA Applied Aerodynamics Conference, Dallas, Texas, 17-21 June 2019.

[21] Spalart, P. and Allmaras, S., "A One-equation Turbulence Model for Aerodynamic Flows," AIAA-92-0439, 1992.

[22] Spalart, P., Deck, S., Shur, M., and Squires, K., "A new Version of Detached-Eddy Simulation, Resistant to Ambiguous Grid Densities," *Theoretical and Computational Fluid Dynamics*, Vol. 20, 2006, pp. 181–195.

[23] Spalart, P. R., "Young-Person's Guide to Detached-Eddy Simulation Grids," NASA/CR-2001-211032, 2001.

[24] Spalart, P., Jou, W.-H., Strelets, M., and Allmaras, S., "Comments on the Feasibility of LES for Wings, and on a Hybrid RANS/LES Approach," Advances in DNS/LES, 1st AFOSR Int. Conf. on DNS/LES, Greyden Press, Columbus, H., Aug. 4-8, 1997.

[25] Yang, Y.-C. and Zha, G.-C., "Simulation of Airfoil Stall Flows Using IDDES with High Order Schemes," AIAA Paper 2016-3185, AIAA AVIATION 2016, 46th AIAA Fluid Dynamics Conference, Washington, D.C., 13-17 June 2016 , 2016.

[26] Patel, P. and Zha, G.-C., "Improved Delayed Detached Eddy Simulation of Separated Flow," AIAA Paper-2020-3013, AIAA Aviation 2020 Forum, Virtual Event, June 15 - 19, 2010.

[27] Patel, P. and Zha, G.-C., "Improved Delayed Detached Eddy Simulation of AGARD Wing Flutter with Fully Coupled Fluid-Structure Interaction," AIAA Paper 2021-0365, AIAA SciTech Forum, VIRTUAL EVENT, 11-15, 19-21 January 2021.

[28] Im, H-S. and Zha, G-C., " Delayed Detached Eddy Simulation of Airfoil Stall Flows Using High Order Schemes ," *ASME Journal of Fluids Engineering*, 2014, pp. DOI: 10.1115/1.4027813.

[29] Gan, J.-Y., Im, H.-S., Chen, X.-C., Zha, G.-C., and Pasiliao, C. L., "Delayed detached Eddy simulation of wing flutter boundary using high order schemes," *Journal of Fluids and Structures*, Vol. 71, 2017, pp. 199–216.

[30] Yang, Y.-C. and Fernandez, M. and Zha, G.-C., "Improved Delayed Detached Eddy Simulation of Super-Lift Flow of Co-Flow Jet Airfoil," AIAA Paper 2018-0314, AIAA SciTech Forum, 2018 AIAA Aerospace Sciences Meeting, Kissimmee, FL, 8-12 January 2018.

[31] Jameson, A., "Time Dependent Calculations Using Multigrid with Applications to Unsteady Flows Past Airfoils and Wings," AIAA Paper 91-1596, 1991.

[32] Shen, Y.-Q. and Zha, G.-C. and Wang, B.-Y., " Improvement of Stability and Accuracy of Implicit WENO Scheme," *AIAA Journal*, Vol. 47, No. 2, 2009, pp. 331–344.

[33] Shen, Y.-Q. and Zha, G.-C. and Chen, X.-Y., " High Order Conservative Differencing for Viscous Terms and the Application to Vortex-Induced Vibration Flows," *Journal of Computational Physics*, Vol. 228(2), 2009, pp. 8283–8300.

[34] Shen, Y.-Q. and Zha, G.-C. , " Improvement of the WENO Scheme Smoothness Estimator," *International Journal for Numerical Methods in Fluids*, Vol. 64, 2010, pp. DOI:10.1002/fld.2186.

[35] Zha, G.-C., Shen, Y., and Wang, B., "An improved low diffusion E-CUSP upwind scheme ," *Journal of Computer & Fluids*, Vol. 48, 2011, pp. 214–220.

[36] Zha, G.-C. and Bilgen, E., "Numerical Solutions of Euler Equations by Using a New Flux Vector Splitting Scheme," *International Journal for Numerical Methods in Fluids*, Vol. 17, 1993, pp. 115–144.

[37] Zha, G.-C. and Bilgen, E., "Numerical Study of Three-Dimensional Transonic Flows Using Unfactored Upwind-Relaxation Sweeping Algorithm," *Journal of Computational Physics*, Vol. 125, 1996, pp. 425–433.

[38] Wang, B.-Y. and Zha, G.-C., "A General Sub-Domain Boundary Mapping Procedure For Structured Grid CFD Parallel Computation," *AIAA Journal of Aerospace Computing, Information, and Communication*, Vol. 5, No.11, 2008, pp. 2084–2091.

[39] Shen, Y.-Q. and Zha, G.-C., "Large Eddy Simulation Using a New Set of Sixth Order Schemes for Compressible Viscous Terms ," *Journal of Computational Physics*, Vol. 229, 2010, pp. 8296–8312.

[40] Boling, J., Zha, G.-C., and Altman, A., " Numerical Investigation of Wingtip Vortices of Coflow Jet Active Flow Control Wings," AIAA Aviation Forum 2020, Virtual Event, 15-19 June, 2020.

[41] McBreen, B., Butler, E., and Zha, G.-C., "Analysis of Wall Jet Flow in EAPG with Super-Lift Coefficient," Proceedings of AIAA Scitech 2024 Forum. Orlando, FL, 8-12 Jan 2024.

[42] Xu, K.-W. and Zha, G.-C., "DESIGN OF HIGH SPECIFIC SPEED MIXED FLOW MICRO-COMPRESSOR FOR CO-FLOW JET ACTUATORS," ASME Paper GT-2019-90980, ASME Turbo Expo 2019, Turbomachinery Technical Conference and Exposition,Phoenix, Arizona, USA, June 17-21, 2019.

[43] Barrios, P., Ren, Y., and Zha, G.-C., "Simulation of 3D Co-Flow Jet Airfoil Control with Micro-Compressor Actuator at High Angles of Attack," AIAA Paper-2023-4208, AIAA AVIATION 2023 Forum, San Diego, CA, 12-16 June 2023.

[44] Barrios, P., Ren, Y., and Zha, G.-C., "Simulation of 3D Co-Flow Jet Airfoil with Integrated Micro-Compressor Actuator at Different Cruise Mach Numbers," AIAA Paper-2023-2118, AIAA SCITECH 2023 Forum, National Harbor, MD, 23-27 January 2023.

[45] McBreen, B., Yang, Y., and Zha, G.-C., "Improved Delayed Detached Eddy Simulation of Co-Flow Jet Flow Control with Enthalpy Effects," Proceedings of AIAA Scitech 2024 Forum. Orlando, FL, 8-12 Jan 2024.